

Genome-wide CRISPR screens identify novel regulators of wild-type and mutant p53 stability

YiQing Lü^{1, 2}, Tiffany Cho^{1,2}, Saptaparna Mukherjee³, Ahmad Malik^{1,2}, Nicolas S. Gonzalez-Foutel⁴, Carmen Florencia Suarez⁴, Dzana Dervovic¹, Robin Hyunseo Oh^{1,2}, Ellen Langille^{1, 2}, Khalid N. Al-Zahrani¹, Zhen Yuan Lin¹, Ricky Tsai¹, Varda Rotter³, Patricia Ashton-Prolla⁵, Lucia B. Chemes⁴, Jason Moffat^{2,6}, Anne-Claude Gingras^{1,2}, Moshe Oren³, Daniel Durocher^{1,2} and Daniel Schramek^{1,2}*

¹ Centre for Molecular and Systems Biology, Lunenfeld-Tanenbaum Research Institute, Mount Sinai Hospital, Toronto, Ontario, Canada

² Department of Molecular Genetics, University of Toronto, Toronto, Ontario, Canada

³ Department of Molecular Cell Biology, Weizmann Institute of Science, Rehovot, Israel

⁴ Instituto de Investigaciones Biotecnológicas (IIBiO-CONICET), Universidad Nacional de San Martín, Buenos Aires, Argentina

⁵ Departamento de Genética, UFRGS and Serviço de Genética Médica HCPA, Porto Alegre, Brasil

⁶ Donnelley Centre, Toronto, Ontario, Canada.

* Correspondence and requests for materials should be addressed to Daniel Schramek

Daniel Schramek, PhD
Lunenfeld-Tanenbaum Research Institute
Mount Sinai Hospital
Toronto, Ontario, Canada M5G 1X5
Phone: +1 416 586-4800
Fax: +1 416 586-8869
schramek@lunenfeld.ca

Abstract

Tumour suppressor p53 (*TP53*) is the most frequently mutated gene in cancer. Several hotspot p53 mutants not only lose tumour suppressive capabilities, but also function in a dominant-negative manner, suppressing canonical wild-type p53 function. Furthermore, some hotspot p53 mutants promote oncogenesis by gain-of-function mechanisms. Levels of p53 are regulated predominantly through regulation of protein stability and while wild-type p53 is normally kept at very low levels at steady-state, p53 mutants are often stabilized in tumours, which may be vital for their oncogenic properties. Here, we systematically profiled the factors that regulate protein stability of wild-type and mutant p53 using marker-based genome-wide CRISPR screens. We found that most proteins that regulate wild-type p53 also regulate a subset of p53 mutants with the exception of p53 R337H regulators, which are largely private to this mutant. Mechanistically, we identified FBXO42 as a novel positive regulator of a subset of p53 mutants comprising R273H, R248Q and R248W. We show that FBXO42 acts together with CCDC6 to regulate USP28-mediated p53 stabilization. Our work also identifies C16orf72 as a negative regulator of the stability of wild-type p53 and of all p53 mutants tested. *C16orf72* is amplified in breast cancer, and we show that *C16orf72* regulates p53 levels in mammary epithelium of mice and its overexpression results in accelerated breast cancer with reduced p53 levels. Together, this work provides a network view of the processes that regulate p53 stability, which might provide clues for reinforcing wild-type p53 or targeting mutant p53 in cancer.

Introduction

Approximately half of all tumours harbor mutations in the p53 (*TP53*) gene, making *TP53* the most commonly mutated gene in cancer¹⁻⁴. The majority of these mutations are missense mutations, most of which not only deprive p53 of its tumour suppressor activities, but might also function in a dominant-negative manner, suppressing canonical p53 functions upon oligomerization with wild-type p53⁵⁻⁹. Some missense mutations also confer a so-called gain-of-function (GOF) phenotype, converting mutant p53 into a cancer-promoting protein that renders cancer cells more malignant by increasing growth rate, motility, invasion, drug resistance and tumorigenicity, while reducing the apoptotic rate^{1, 3, 10-17}. Importantly, compared to tumours with wild-type p53 or those lacking p53 altogether, tumours expressing GOF mutant p53 are more invasive, metastatic, and proliferative, and display increased genome instability and chemoresistance in mouse and man^{3, 12, 18-23}. Two main classes of p53 hotspot mutations have been distinguished – those that affect residues directly involved in protein-DNA interaction, such as R248 or R273 ('contact mutants'), and those that affect residues involved in stabilizing the tertiary structure of the protein, such as R175, G245, R249 and R282 ('conformational' or 'structural' mutants).

Germline *TP53* mutations also exist, often target the same hotspot residues, and are the underlying cause of Li-Fraumeni Syndrome, which predisposes to a wide spectrum of early-onset cancers. In Brazil, the *TP53* R337H founder mutation exists at high frequency and represents the most common germline *TP53* mutation reported to date²⁴. Interestingly, unlike most hotspot mutations, this mutation is not located in the DNA binding domain of p53 but in the oligomerization domain and disrupts p53 oligomerization.

While wild-type p53 protein expression is tightly regulated and kept at a low under homeostatic condition, mutant p53 is often stabilized and highly overexpressed in tumours, which is thought to be required for mutant p53 to exert its oncogenic effects. In fact, strong immunohistochemical staining patterns of nuclear p53 still serve as a surrogate marker for *TP53* mutations in the clinic^{25, 26}. Interestingly, knock-in mouse models of p53 and Li-Fraumeni patients carrying germline p53 GOF mutations highly express mutant p53 specifically in tumour cells, but show low or undetectable levels of mutant p53 in the surrounding, phenotypically normal tissues^{3, 18, 19, 27}. This observation indicates that mutant p53 is not intrinsically stable and that its levels are kept in check in healthy cells, but that this regulation is perturbed in cancer^{3, 18, 19}. The stability of wild-type p53 is regulated mainly through MDM2/4-mediated ubiquitination and degradation²⁸⁻³⁰ but little is known about the factors that regulate mutant p53 stability.

Here, we employed functional genomics and proteomics approaches to systematically profile the processes that regulate the stability of wild-type, as well as of the most common p53 mutants that collectively account for ~50% of all mutant p53²⁴. These screens identified 864 genes whose loss either

increases or decreases the stability of p53 mutants. Mining this dataset, we report that the FBXO42-CCDC6-USP28 axis acts as a positive regulator of mutant p53 stability and the C16orf72-HUWE1-USP7 axis acts as a negative regulator of p53 stability.

Results

A fluorescence-based p53 stability reporter system

To monitor p53 stability at the single-cell level, we generated a lentiviral protein stability reporter (**Fig 1a**) consisting of a p53-mClover-P2A-mRFP cassette that permits translation of a mClover-p53 protein fusion and a red fluorescent RFP protein from the same mRNA transcript, similar to previous protein stability reporters^{31, 32}. The p53-mClover fusion assesses p53 stability, while mRFP serves as an internal control to monitor expression of the bicistronic transgene (**Fig. 1a**).

To benchmark this reporter, we used an hTERT-immortalized retinal pigment epithelium-1 (RPE1) cell line that expresses Cas9 and was previously used in CRISPR screens³³. We used a RPE1 subclone in which the gene encoding p53 was knocked out by gene editing³⁴ and generated isogenic lines expressing stability reporters containing either wild-type p53 or 8 of the most common hotspot p53 mutations (R175H, G245S, R248Q, R248W, R249S, R273H, R282W, and R337H). As a control, we also generated a cell line expressing the mClover-P2A-RFP cassette without p53. We observed that cells transduced with p53 G245S, R248Q, R248W or R273H exhibited bimodal distribution of p53 levels, with one subset expressing hardly any p53 and the other subset expressing higher levels of p53. This pattern of p53 protein expression was observed with both structural (G245S) and contact (R248Q, R248W, R273H) p53 mutants (**Fig. 1b**). Such bimodal distribution was also observed in lymphoma cell lines expressing endogenous p53 R248Q, R248W or R273H mutants³⁵ and thus likely reflects the intrinsically unstable nature of mutant p53²⁷. In line with previous data showing that MDM2 promotes the degradation of wild-type and some mutant p53^{27, 29, 36}, treatment with the MDM2 inhibitor Nutlin-3a elevated the levels of wild-type p53 and the p53 mutants G245S, R248Q, R248W, and R273H, while R175H, R249S, R282W and R337H did not respond to Nutlin-3a (**Fig 1b**). Upon removal of Nutlin-3a, levels of wild-type p53 and mutant p53 returned to baseline levels, re-establishing the uni- or bimodal distribution of the starting population (**Fig. 1b**). Similarly, we observed that irradiation led to significantly increased levels of p53 mutants (G245S, R248Q, R248W, R273H) with the exception of p53 R175H, R249S, R282W, and R337H (**Suppl. Fig. 1a**), further indicating that several p53 mutants and especially the contact p53 mutants are regulated by the same machinery that regulates wild-type p53. In line with these data, CRISPR/Cas9-mediated ablation of MDM2 elevated the p53^{R273H}-mClover, which could be reversed by ectopically re-expressing MDM2, further validating our reporter system (**Fig. 1c**).

Genome-wide CRISPR screens identifies regulators of wild-type and mutant p53 stability

To identify regulators of p53 stability, we performed genome-wide pooled CRISPR screens in RPE1-hTERT Cas9 cells expressing either the control mClover-P2A-RFP cassette or the stability reporters for p53 wild-type, R175H, G245S, R248Q, R273H, or R337H. We used the TKOv3 lentiviral sgRNA library, which contains 70,948 guides (~4 guides/gene) targeting 18,053 protein-coding genes and 142 control sgRNAs targeting EGFP, LacZ and luciferase³⁷. We transduced the reporter lines at 200X coverage, selected for infected cells and isolated cell populations expressing low or high p53-mClover by flow cytometry (**Fig. 1d**). For reporter lines with a unimodal p53 distribution, we sorted cells with the lowest and highest 15% of p53-mClover expression, and for lines with a bimodal p53 distribution, we isolated the lower and the upper populations. The 7 cell lines were screened in duplicates at a minimum and we observed a good reproducibility between sgRNA abundance in the replicates ($r = 0.44 - 0.71$)³³ (**Suppl. Fig. 1b**).

For gene-level depletion/enrichment, we calculated a normalized z-score (NormZ) of the low and high p53-mClover populations, combining multiple sgRNAs per gene. Negative NormZ scores represent genes whose inactivation leads to decreased p53 levels (i.e. positive regulators of p53 stability), whereas positive NormZ scores represent genes whose inactivation leads to increased p53 levels (i.e. negative regulators of p53 stability). As expected, sgRNAs targeting p53 and mClover were the most depleted sgRNAs, while sgRNAs targeting MDM2 or MDM4 were among the most enriched sgRNAs in the p53-high populations. Other known positive regulators of p53 such as ATM, USP28, TTI1/2, TP53BP1, or CHEK2 and negative regulators of p53 stability such as USP7, HUWE1 or PPM1D/G also scored in several p53 wild-type or mutant screens, further validating the screens (**Fig. 1e and f** and **Suppl. Fig. 2a-d** and **Suppl. Table 1**). Unsupervised clustering of the screens showed that p53 wild-type, G245S, R248Q, R273H mutants clustered closely together, while R175H p53 and p53 R337H showed distinct profiles (**Fig. 1g**).

To identify hits, we selected genes with a NormZ values +/- 3, a false discovery rate (FDR) lower than 0.5 and excluded genes that also affected the negative control mClover-P2A-mRFP reporter. These cutoffs identified 292 and 548 genes, whose loss led to decreased and increased p53 levels, respectively. While most genes regulated stability of wild-type and several p53 mutants, we also identified p53 wild-type- and p53 mutant-specific regulators (**Fig. 1h**). For example, wild-type p53 levels were specifically sensitive to perturbation of the 20S and 19S proteasomal subunits, consistent with the high protein turn-over of p53. This is in contrast to the levels of some mutant p53 proteins, such as R273H and R248Q, whose levels were not significantly affected upon genetic ablation of proteasome subunits (**Suppl. Fig. 2e**). In addition, of the 292 hits whose loss caused p53 destabilization, the vast majority (182 genes) regulated only p53 R337H. Conversely, of the 548 hits whose loss led to p53 stabilization, only a small subset (52 genes) regulated p53 R337H (**Fig. 1h, Suppl. Fig. 1B**). These data suggest that p53 R337H is controlled by mechanisms that are different from those modulating wild-type p53 and all other p53 mutants tested.

FBXO42-CCDC6 axis regulates wild-type and mutant p53 stability

One of the strongest hits whose loss led to decreased p53 levels (i.e. represents a positive p53 regulator) in the R273H and R248Q screens was *FBXO42* (NormZ value of -4.05 and -5.65 for R273H and R248Q, respectively), coding for F-Box Protein 42, which functions as a substrate-recognition subunit of an SCF (SKP1-CUL1-F-box protein)-type E3 ubiquitin ligase complex. Analysis of the Dependency Map (DepMap) project³⁸ indicated that the genetic dependency profile of *FBXO42* correlated with that of p53 and its activators *CHEK2*, *TP53BP1*, *ATM* and *USP28* and was inversely correlated with those of negative p53 regulators such as *MDM2*, *MDM4*, *PPM1G* and *USP7* (**Fig. 2a, b**), strongly suggesting a functional connection to the p53 pathway. The strongest genetic co-dependency of *FBXO42* and one of the strongest correlations across all genes and cell lines, was with *CCDC6*, which encodes a coiled-coil domain containing protein (**Fig. 2a and b**). *CCDC6* shows a similarly strong co-dependency with the p53 pathway in DepMap and loss of *CCDC6* caused phenotypes similar to those associated with the loss of *FBXO42* in our screens, i.e. resulting in decreased p53 R273H and R248Q levels (**Fig. 2c and Suppl. Table 1**).

We used two independent sgRNAs with good on-target efficacy to corroborate the effect of *FBXO42* and *CCDC6* loss on p53 stability and used sgRNAs targeting the *AAVS1* locus as control (**Suppl. Fig. 2f**). We observed significantly reduced R273H, R248Q and R248W p53-mClover levels but failed to see significant effects on wild-type, R175H, G245S or R337H p53-mClover levels (**Fig. 2d and Suppl. Fig. 3a**), indicating specificity for some p53 mutants. The difference in p53 levels was even more apparent upon irradiation (**Suppl. Fig. 3b-d**) and in single cell knock-out clones (**Fig. 2e**). We also tested whether proteasomal degradation is involved in *FBXO42/CCDC6*-mediated regulation of mutant p53. Inhibition of the proteasome by MG132 increased mutant p53 levels in *FBXO42* and *CCDC6* knock-out cells as assessed by WB analysis and flow cytometry (**Fig. 2e and Suppl. Fig. 3e**). Importantly, genetic ablation of *FBXO42* also reduced the levels of p53 in the pancreatic cancer cell line PANC-1, which is homozygous for p53 R273H³⁹ (**Fig. 2f**), without affecting *TP53* mRNA expression, confirming that *FBXO42* acts on p53 via posttranscriptional regulation (**Suppl. Fig. 3f**).

To test for a potential epistatic relationship between *FBXO42* and *CCDC6*, we used isogenic *FBXO42*-knockout (Δ *FBXO42*), *CCDC6*-knockout (Δ *CCDC6*) and *AAVS1*-targeted control RPE-1 p53^{R273H}-mClover reporter cell lines (**Fig. 2e**). As expected, p53^{R273H}-mClover levels in Δ *FBXO42* and Δ *CCDC6* could be partially rescued by re-expressing *FBXO42* or *CCDC6*, respectively. Interestingly, while expression of *FBXO42* did not rescue p53^{R273H}-mClover levels in Δ *CCDC6* cells, we found that expression of *CCDC6* partly rescued mutant p53 levels in Δ *FBXO42* cells (**Fig. 2g**), suggesting that *FBXO42* may function upstream of *CCDC6*.

Using *FBXO42* truncation mutants, we found that both the Kelch and F-Box domains are required to promote p53 R273H stabilization, indicating that *FBXO42*'s ability to stabilize p53 R273H is dependent

on both its substrate binding domain and by its incorporation into an SCF complex, likely to promote SKP1/CUL1-mediated ubiquitination of an as-yet unidentified substrate (**Fig. 2h** and **Suppl. Fig. 3g, h**). Together, these data indicate that FBXO42 and CCDC6 function as positive post-translational regulators of wild-type p53 and several p53 mutants in a ubiquitination-dependent manner.

Mapping of the FBXO42-CCDC6 and mutant p53 interaction network

To investigate how FBXO42-CCDC6 regulates p53 stability, we identified vicinal proteins by proximity-dependent biotinylation coupled to mass spectrometry (BioID)⁴⁰⁻⁴³ using inducible expression of biotin ligase (BirA*)-tagged FBXO42, CCDC6 or p53 R273H in HEK293 Flp-In T-REx cells. Given that proteasome-sensitive nature of this regulatory circuit, we performed these BioID experiments in the absence or presence of MG132. Consistent with its role as an SCF-E3 ligase, the top interactors for FBXO42 were CUL1 and SKP1. FBXO42 BioID also enriched for CCDC6, p53 itself as well as proteins known to regulate p53 such as HUWE1 (**Fig. 3a**, **Suppl. Table 2**). p53 R273H proximal proteins included known p53 interactors such as MDM2, BRCA2, USP28, TP53BP1, PPM1G, BLM, ATRX and PML (**Fig. 3a**). In addition, endogenous CCDC6 co-immunoprecipitated (co-IP) with endogenous p53 R273H and the reciprocal co-IP also found endogenous mutant p53 interacting with V5-tagged CCDC6 in PANC-1 cells (**Fig. 3b** and **Suppl. Fig. 4a**). In further support of this interaction, proximity ligation assay (PLA) showed that CCDC6 and p53 R273H interact with each other predominantly in the nucleus (**Fig. 3c**). Using *in vitro* binding assays of recombinant proteins, we detected a direct interaction between FBXO42 Kelch domains 1-3 and the core DNA-binding domain of p53 R273H (**Fig. 3d**, **Suppl. Fig. 3h**). Together, these data show that R273H p53 interacts with both its regulators CCDC6 and FBXO42 and indicates a potential formation of a higher order complex that regulates p53 stability.

FBXO42-CCDC6 regulates p53 via USP28

To identify genetic determinants of FBXO42/CCDC6-mediated p53 R273H stabilization, we performed genome-wide CRISPR screens using isogenic $\Delta FBXO42$, $\Delta CCDC6$ or control RPE1 p53^{R273H}-mClover-P2A-RFP reporter cell lines. This allowed us to systematically map genetic perturbations that regulate p53 R273H stability depending on the presence of FBXO42 and CCDC6 (**Fig. 3e and f**). Most genes such as *MDM2*, *MDM4*, *USP7*, *CSNK1A1*, *ATM* or *TTI* retained their function in regulating p53 stability in $\Delta FBXO42$ or $\Delta CCDC6$ RPE1 cells. As expected for genes in the same pathway and based on our previous data, *CCDC6* did not score in the $\Delta FBXO42$ screen (nor did *FBXO42*) and *FBXO42* did not score in the $\Delta CCDC6$ screen (nor did *CCDC6*). Interestingly, we identified one F-Box protein coding-gene, *FBXL18*, which gained the ability to reduce p53^{R273H}-mClover levels in $\Delta FBXO42$ or $\Delta CCDC6$ RPE1 cells but did not have an effect when lost in parental RPE1 wild-type cells, suggesting that FBXL18 may compensate for the loss of FBXO42/CCDC6 (**Fig. 3e and f**). In addition, loss of *USP28*, whose perturbation led to the strongest

reduction in p53^{R273H}-mClover levels in wild-type RPE1, had no effect on p53^{R273H}-mClover levels in the Δ *FBXO42* screen, and only a weak effect on p53^{R273H}-mClover levels in the Δ *CCDC6* screen, indicating that USP28 may function in the same pathway as FBXO42/CCDC6 (**Fig. 3e and f**). We corroborated these genetic interactions and showed that concomitant loss of *USP28* in Δ *FBXO42* or Δ *CCDC6* RPE1 cells has no effect on p53^{R273H}-mClover levels (**Suppl. Fig. 4b**). Interestingly, loss of *FBXO42* or *CCDC6* resulted in decreased levels of nuclear USP28 as shown by nuclear/cytoplasmic fractionation as well as immunofluorescence (**Fig. 3g and Suppl. Fig. 4c**). Importantly, ectopic expression of either FBXO42 or CCDC6 not only rescued the USP28 and R273H p53 levels in Δ *FBXO42* or Δ *CCDC6* RPE1 cells but also led to increased USP28 levels in the parental RPE1 cells, concomitant with a slight upregulation of p53 levels (**Fig. 3h**). Genetic ablation of *FBXO42* or *CCDC6* in PANC-1 cells also reduced USP28 protein abundance, without affecting USP28 transcript levels (**Fig. 3i and Suppl. Fig. 4d**), indicating that the post-translational regulation of USP28 by FBXO42/CCDC6 is not unique to RPE1 cells. Next, we generated Δ *USP28* p53^{R273H}-mClover RPE1 cells and assessed how overexpression of FBXO42 and CCDC6 impacted p53 R273H levels (**Suppl. Fig. 4e**). While expressing USP28 rescued p53 R273H levels, overexpressing FBXO42 or CCDC6 in Δ *USP28* cells had no effect, indicating that FBXO42/CCDC6 act via USP28. Moreover, we found that USP28 overexpression rescued mutant p53 levels in Δ *FBXO42* or Δ *CCDC6* RPE1 cells, indicating that USP28 is downstream of FBXO42/CCDC6 (**Suppl. Fig. 4e**). Together, these data indicate that FBXO42/CCDC6 control mutant p53 levels via USP28.

Synthetic viability screen maps positive regulators of p53

To better understand the genes whose loss leads to p53 stabilization (i.e. that act as p53 negative regulators), we first performed pathway analysis using gProfiler (**Fig. 4a and Suppl. Table 3**). Gene sets associated with cellular response to stress, extracellular stimuli or hypoxia, cell cycle, mitosis, stabilization of p53 and p53-dependent and -independent DNA Damage Responses were significantly enriched in the 547 hits that result in higher p53 levels. Enrichment was also found for genes involved in regulation of nonsense-mediated decay and programmed cell death. Interestingly, metabolism of RNA and rRNA modification in the nucleus and cytosol were the most significantly enriched categories. This functional group was also enriched in various other screens done to identify genes that cause genomic instability or modulate responses to ionizing or UV radiation, or screens for ATM/ATR substrates⁴⁴⁻⁴⁷, indicating that RNA metabolism is tightly interconnected with DNA damage responses. Together, this data indicates that stability of mutant p53 is to a large extent regulated by the physiological machinery that regulates stress-induced wild-type p53 stability. However, this data may also indicate that most of the hits whose loss leads to p53 stabilization might regulate p53 indirectly by triggering a stress response.

As an alternative approach to identify regulators of p53, we sought to exploit the concept of synthetic viability, which describes a genetic interaction where viability of one genetic mutation is determined by the presence of a second genetic mutation⁴⁸. The mutations in *MDM2* and *TP53* display a synthetic viability interaction, as the embryonic and cellular lethality associated with the loss of *MDM2* is completely rescued in a p53 null background⁴⁹. To identify the full repertoire of genes that are synthetic viable with p53, we performed genome-wide CRISPR screens in isogenic p53-proficient and -deficient RPE1 cell lines. Synthetic viable interactions were defined as genes that had high Bayes factors (BF) in p53-proficient cells, indicating essentiality, but negative BF values in the p53-deficient cells (**Suppl. Table 4**). As expected, the known negative p53 regulators *MDM2*, *MDM4*, *USP7*, *PPM1D* (encoding *WIP1*) all scored highly as synthetic viability hits in the screen. In addition, pathway analysis of the top 150 scoring genes using PANTHER⁵⁰ revealed enrichment of genes involved in the p53 pathway and the related Ubiquitin proteasome pathway (**Fig. 4c** and **Suppl. Table 5**).

To delineate high confidence p53 regulators, we searched for hits that scored in both the p53 synthetic viability and the p53 reporter screens. 17 out of the 53 top-scoring genes in the synthetic viability screen also scored in the p53 reporter screens. In addition to the well-known p53 regulators (*MDM2/4*, *USP7*, *PPM1D/G*), *ZNF574*, *APEX2*, *BRAP*, *NONO*, *TCOF1*, *OTUD5*, *UBR5*, *LSM12*, *DSCC1*, *C14orf80*, *EXOSC1*, and *C16orf72* scored prominently in both screening formats (**Fig. 4d**; and **Suppl. Table 1&4**).

C16orf72 (also known as *TAPRI*) was previously identified in a screen for genes that altered sensitivity to telomere attrition and was shown to buffer against p53 activation in response to telomere erosion⁵¹. Moreover, we recently identified *C16orf72* in a screen that analyzed genetic vulnerabilities to ATR inhibition⁵². In addition, analysis of coessentiality across 789 cancer cell lines from the DepMap project showed a striking association between *C16orf72* and several positive and negative p53 regulators (**Fig. 4e** and **f**)^{51, 53}. Together, these data identified *C16orf72* as a candidate negative regulator of p53 stability.

C16orf72 is a regulator of wild-type and mutant p53 stability

To validate the genetic interaction between *TP53* and *C16orf72*, we performed clonogenic survival assays. Loss of *C16orf72* resulted in decreased cell viability and relative cellular fitness selectively in the *TP53*^{+/+} background but had no impact in the p53-deficient isogenic counterpart, indicating synthetic viability (**Fig. 5a**). Loss of *C16orf72* also caused an increased in p53 levels for wild-type as well as all tested p53 mutants (**Fig. 5b, c** and **Suppl. Fig. 5a**).

To gain further insight into the putative functions of *C16orf72*, we performed affinity purification coupled to mass spectrometry (AP-MS) on FLAG-tagged *C16orf72*. This identified HUWE1 as a prominent interactor of *C16orf72*, in line with previous findings⁵¹ (**Fig. 5d** and **Suppl. Table 6**). HUWE1, a known E3 ubiquitin ligase for p53, scored as a hit in our marker-based p53 stability screens and showed the strongest

co-essentiality in DepMap (**Fig. 2C and 5e**). However, we did not identify HUWE1 as a hit in our synthetic viability screen, and siRNA mediated knock-down of HUWE1 only led to a slight increase in p53 levels compared to loss of other known negative p53 regulators such as MDM2 or USP7 (**Fig. 5e**). Together, these data indicate that mechanisms other than HUWE1 might be involved in the stabilization of p53 following *C16orf72* loss or that the HUWE1-dependent modulation of p53 is complex, masking its potential role alongside *C16orf72* in that cell line.

The second most significant co-essential gene of *C16orf72* in DepMap was *USP7* (**Fig. 4f and g**), which also scored as a synthetic viable p53 interaction as well as a strong p53 stability regulator in our CRISPR screens (**Fig. 2c and 4b**). To test a potential functional relationship between *C16orf72* and *USP7*, we performed co-immunoprecipitation experiments and found that FLAG-tagged full-length *USP7* can interact with HA-tagged *C16orf72* (**Fig. 5f**). Together, this indicates that *C16orf72* might regulate p53 via *USP7*.

C16orf72 functions as oncogene and regulates p53 stability in the mammary gland

Strikingly, the *USP7* gene lies directly adjacent to *C16orf72* and both genes are commonly co-amplified in up to 7.6% of cancers as well as being co-gained in up to 53% of cases ($p < 0.001$; **Suppl. Fig. 5b and c**). Invasive breast cancer showed the highest level of amplification and gains of the *USP7/C16orf72* locus in up to 55% of tumors ($p < 0.001$; **Fig. 6a**), suggesting that these two co-amplified negative p53 regulators might cooperate in modulating p53 levels in cancer.

To test the role of *C16orf72* *in vivo*, we first conducted multicolour competition assays in the mammary glands of LSL-Cas9-GFP mice. Intraductal injection of lentiviral particles expressing Cre, RFP and a sgRNA cassette targeting *Mdm2* or *C16orf72* led to a drastic reduction of mammary epithelial cells of LSL-Cas9-GFP mice when compared to a control lentivirus expressing Cre, BFP and an sgRNA targeting the inert *Tigre* locus. The reduced cell viability was dependent on p53, as conditional p53 knock-out mice (*Trp53^{fl/fl}*; LSL-Cas9-GFP) did not show an overt phenotype (**Fig. 6b**).

Conversely, overexpression of *C16orf72* led to a significant reduction in p53 R273H levels in RPE1 cells (**Fig. 6c**) and levels of wild-type p53 expression in human *Pik3ca^{H1047R}*-mutant mammary epithelial MCF10A cells (**Fig. 6d**). This led us to ask whether overexpression of *C16orf72* can decrease the latency of *Pik3ca^{H1047R}*-driven mammary tumours. Of note, we observed that loss of p53 cooperates with *Pik3ca^{H1047R}* to accelerate mammary tumour initiation (**Suppl. Fig. 5d**)^{54, 55}. Like loss of p53 or overexpression of *Mdm2*, intraductal injection of lentiviral particles expressing Cre and *C16orf72* or *USP7* significantly reduced the latency of *Pik3ca^{H1047R}*-driven mammary tumour development (**Fig. 6e**). Importantly, *C16orf72* overexpressing tumours and hyperplastic mammary epithelium showed a drastic reduction in p53 levels compared to Ruby control lesions (**Fig. 6f**). Together these data show that *C16orf72* overexpression leads to decreased p53 protein levels *in vitro* and *in vivo* and leads to accelerated tumour formation.

Discussion

Over 22 million cancer patients today carry *TP53* mutations, the majority of which are missense mutations, often resulting in elevated expression of mutant p53 proteins². Lowering mutant p53 expression can reduce tumour growth and metastasis and trigger tumour regression⁵⁶⁻⁵⁸, suggesting that tumours become addicted to mutant p53. Targeting factors that regulate mutant p53 stability or reactivate wild-type p53 function might therefore constitute a viable therapeutic strategy.

We therefore conducted genome-wide CRISPR screens in isogenic RPE1 cells expressing protein stability reporters for wild-type p53 and five of the most common p53 mutants. Unsupervised hierarchical clustering showed that most hotspot mutant p53 proteins (R175H, G245S, R248Q, R273H) are regulated by a common molecular network, which is to a certain degree distinct from wild-type p53. Interestingly, the Brazilian founder mutation R337H, which is located in the oligomerization domain and is the only mutation in our study that resides outside of the DNA binding domain, behaved drastically differently to the other hotspot mutations and wild-type p53. As such, it will be interesting to further elucidate the molecular underpinnings of why some mutations behave like wild-type p53, while others do not. Together, these data provide a comprehensive map of genes that regulate wildtype and mutant p53 protein stability and might have implications for the development of agents that target mutant p53 in cancer therapy.

We next characterized two mutant p53 regulators, FBXO42 and CCDC6, and provided strong genetic evidence that FBXO42 in conjunction with CCDC6 are novel regulators of certain p53 mutants. FBXO42 was previously reported as a negative regulator of wild-type p53 and shown to bind a phosphodegron on p53, leading to its proteasomal degradation in U2OS cells⁵⁹. The COP9 signalosome-associated kinase was found to mediate the phosphorylation of p53's core DNA binding domain, which was required to allow FBXO42 binding and ubiquitination⁶⁰. We found no significant effect of FBXO42 on wild-type p53 or R175H, G245S or R337H p53, but genetic ablation of FBXO42 caused destabilization of p53 R273H, R248Q and R248W. This is consistent with the co-dependencies of FBXO42 and CCDC6 in DepMap, which clearly align them with positive p53 regulators such as ATM, CHEK2, TP53BP1 and USP28, while they are anticorrelated with negative p53 regulators such as MDM2/4, TTC1 or PPM1G/D. Interestingly, other previously reported regulators of mutant p53 stability such as TRRAP, BAG2 or BAG5 did not score as hits in our screen, suggesting that context may be important for p53 regulation^{35, 61-63}.

Similarly, we found that CCDC6 also regulates the same p53 mutants. Of note, CCDC6 and FBXO42 were recently shown to interact genetically^{64, 65}. We corroborated this interaction data and show that they also interact physically. In addition, we found an interaction between CCDC6 and p53 (by PLA and IP) and a direct interaction between FBXO42's Kelch domains and p53 R273H. Epistasis experiments showed that FBXO42 appears to function upstream of CCDC6 in regulating p53. In addition, we also found that another well-known p53 regulator, BRCA2, interacts with mutant p53 and also surfaced as a FBXO42 vicinal protein and a potential FBXO42 target (Fig. 3a). However, it is still unclear whether these interactions are required to regulate p53 protein levels.

Using further genetic screening in FBXO42- and CCDC6-knockout p53 R273H reporter query lines and additional epistasis experiments, we uncovered a genetic interaction of FBXO42/CCDC6 with USP28. USP28 was originally implicated as a protective deubiquitinating enzyme counteracting the proteasomal degradation of p53, TP53BP1, CHCK2, and additional proteins⁶⁶⁻⁶⁹. USP28 regulates wild-type p53 via TP53BP1-dependent and -independent mechanisms. Concordantly, our data shows that USP28 and TP53BP1 are strong positive regulators of wild-type p53. However, while USP28 was also a strong hit in the mutant p53 R273H screen, TP53BP1 was not, indicating that the effects we see upon loss of USP28 on p53 R273H are independent of TP53BP1. In addition, we found that genetic ablation of FBXO42 or CCDC6 leads to a significant reduction of nuclear USP28 levels, adding further biochemical support to the genetic interaction data. While the exact molecular mechanisms are currently unclear, we provide strong evidence that FBXO42/CCDC6 is required for USP28-mediated regulation of p53 R273H stability, suggesting that interfering with this regulatory circuit could present an avenue to prevent or reduce mutant p53 accumulation in tumours.

USP28 also regulates other important proteins such as MYC by counteracting FBXW7-mediated proteasomal degradation, as well as cJun, Notch1, LSD1, HIF-1a and MDC1⁶⁹. It will be interesting to elucidate whether FBXO42 and CCDC6 also impinge on those cellular pathways or whether there is some selectivity.

Our data also shows that there are many genes whose loss results in increased p53 levels, which presumably is rooted in the fact that any gene loss which causes cellular stress will probably indirectly lead to p53 stabilization. Therefore, we cross-referenced our p53 stability screen with a synthetic viability screen, which revealed a key role of C16orf72 as a negative regulator of wild-type and mutant p53. The role of C16orf72 in a p53 regulatory mechanism is further supported by the mutual exclusivity of *TP53* genetic alteration and *C16orf72* amplification/gains, which is observed in up to 55% of breast cancer genomes. However, the direct implication on the role of *C16orf72* amplification in tumour development is complicated by the fact that the *USP7* gene is located adjacent to the C16orf72 locus, resulting in concurrent amplification of *USP7* and C16orf72. In addition, recurrent *de novo* copy number amplifications encompassing *USP7* and *C16orf72* are also seen in autism spectrum disorder⁷⁰, and the role of p53 and the DNA damage response pathway in neurodegenerative diseases and autism is increasingly recognized^{71, 72}, further indicating a potentially interesting connection.

By generating autochthonous breast cancer mouse models, we could show that overexpression of *C16orf72* or *USP7* independently accelerates *Pik3ca*^{H1047R}-driven mammary tumour formation.

Mechanistically, we show that C16orf72 interacts with USP7 and HUWE1 that are *bone fide* regulators of p53, potentially hinting at how C16orf72 may regulate p53 stability. Our findings are also in line with a recent report showing that C16orf72 is crucial for mediating telomere attrition-induced p53-dependent apoptosis and regulating the effects of ATR inhibition^{51,52}.

In summary, our study provides a rich resource to mine for candidate regulators of wild-type and mutant p53 stability. Moreover, it can serve as a template to reveal regulators of any protein of interest on a genome-wide level.

Supplementary Information contains all Methods, Supplementary Fig. 1-5, Supplementary Fig. legends and Supplementary Tables 1-7.

Acknowledgements. We would like to thank all members of our laboratories as well as, Mikko Taipale, Brian Raught, Yael Aylon, and The Centre for Phenogenomics (TCP) for helpful discussions. We want to thank Henrique Melo, Zheng Luo, Mingkun Wu and Matthew Guo for assistance with data analysis, Annie Bang, Michael Parsons and Dione White in the Lunenfeld-Tanenbaum Research Institute Flow Cytometry Facilities for assistance with FACS, Kin Chan at the Lunenfeld Network Biology Centre for assistance with next generation sequencing, Andrew Elia at the University Health Network for assistance with histology, and Geraldine Mbamalu and Sampath Loganathan for general experiment helps. The FLAG-USP7 construct is a generous gift of Lori Frappier. Research in this work is supported by fundings from the Joint Canada-Israel Research Programme (D.S., M.O., V.R., A.C.G., P.A.P., and L.B.C., CIHR IRDC 384428). D.D was supported by a grant from the Canadian Cancer Society (705644). Y.Q.L. is the recipient of doctoral fellowships from the Canadian Institute of Health Research (CIHR 157921 and MSFSS 431649), Government of Ontario (OGS) and the University of Toronto. D.S. is supported by the Canada Research Chair programme. P.A-P was supported by a scholarship from CNPq (Conselho Nacional de Desenvolvimento Científico e Tecnológico, Brazil, # 307826/2017-1).

Author Contributions. Y.L. performed all p53 stability screens and almost all FBXO42/CCDC6 and C16orf72 mouse experiments. T.C. performed the p53 synthetic viability screens and most of the biochemical C16orf72 experiments. S.M. helped performed CCDC6 IP and PLA experiments. A.M. helped with bioinformatics. R.H.O., E.L. and K.N.A. helped with mouse experiments. Z.Y.L. together with A.C.G. performed mass spectrometry. N.G.F., C.F.S. together with L.B.C. performed FBXO42-p53 binding experiments. V.R. and P.P helped with conceptualization of the project. J.M. helped with CRISPR screens, and D.D.1. and R.T. helped with flowcytometry and RT-PCR experiments. Y.L., T.C., D.D.2, M.O. and D.S. designed the experiments and coordinated the project, and together with Y.L. and D.S. wrote the manuscript.

D.D.1.: Dzana Dervovic; D.D.2.: Daniel Durocher.

Competing interests. All authors declare no competing interests.

References

1. Vogelstein, B., Lane, D. & Levine, A.J. Surfing the p53 network. *Nature* **408**, 307-310 (2000).
2. Petitjean, A. *et al.* Impact of mutant p53 functional properties on TP53 mutation patterns and tumor phenotype: lessons from recent developments in the IARC TP53 database. *Hum Mutat* **28**, 622-629 (2007).
3. Oren, M. & Rotter, V. Mutant p53 gain-of-function in cancer. *Cold Spring Harb Perspect Biol* **2**, a001107 (2010).
4. Freed-Pastor, W.A. & Prives, C. Mutant p53: one name, many proteins. *Genes Dev* **26**, 1268-1286 (2012).
5. Varley, J.M. *et al.* A detailed study of loss of heterozygosity on chromosome 17 in tumours from Li-Fraumeni patients carrying a mutation to the TP53 gene. *Oncogene* **14**, 865-871 (1997).
6. Malkin, D. Li-fraumeni syndrome. *Genes Cancer* **2**, 475-484 (2011).
7. Liu, D.P., Song, H. & Xu, Y. A common gain of function of p53 cancer mutants in inducing genetic instability. *Oncogene* **29**, 949-956 (2010).
8. Chene, P. In vitro analysis of the dominant negative effect of p53 mutants. *J Mol Biol* **281**, 205-209 (1998).
9. Giacomelli, A.O. *et al.* Mutational processes shape the landscape of TP53 mutations in human cancer. *Nat Genet* **50**, 1381-1387 (2018).
10. Weisz, L. *et al.* Transactivation of the EGR1 gene contributes to mutant p53 gain of function. *Cancer Res* **64**, 8318-8327 (2004).
11. Zalcenstein, A. *et al.* Mutant p53 gain of function: repression of CD95(Fas/APO-1) gene expression by tumor-associated p53 mutants. *Oncogene* **22**, 5667-5676 (2003).
12. Blandino, G., Levine, A.J. & Oren, M. Mutant p53 gain of function: differential effects of different p53 mutants on resistance of cultured cells to chemotherapy. *Oncogene* **18**, 477-485 (1999).
13. Peled, A., Zipori, D. & Rotter, V. Cooperation between p53-dependent and p53-independent apoptotic pathways in myeloid cells. *Cancer Res* **56**, 2148-2156 (1996).
14. Muller, P.A. & Vousden, K.H. p53 mutations in cancer. *Nat Cell Biol* **15**, 2-8 (2013).
15. Wolf, D., Harris, N. & Rotter, V. Reconstitution of p53 expression in a nonproducer Ab-MuLV-transformed cell line by transfection of a functional p53 gene. *Cell* **38**, 119-126 (1984).
16. Dittmer, D. *et al.* Gain of function mutations in p53. *Nat Genet* **4**, 42-46 (1993).

17. Eliyahu, D., Raz, A., Gruss, P., Givol, D. & Oren, M. PARTICIPATION OF P53 CELLULAR TUMOR-ANTIGEN IN TRANSFORMATION OF NORMAL EMBRYONIC-CELLS. *Nature* **312**, 646-649 (1984).
18. Olive, K.P. *et al.* Mutant p53 gain of function in two mouse models of Li-Fraumeni syndrome. *Cell* **119**, 847-860 (2004).
19. Lang, G.A. *et al.* Gain of function of a p53 hot spot mutation in a mouse model of Li-Fraumeni syndrome. *Cell* **119**, 861-872 (2004).
20. Liu, G. *et al.* High metastatic potential in mice inheriting a targeted p53 missense mutation. *Proc Natl Acad Sci U S A* **97**, 4174-4179 (2000).
21. Zerdoumi, Y. *et al.* Drastic effect of germline TP53 missense mutations in Li-Fraumeni patients. *Hum Mutat* **34**, 453-461 (2013).
22. Bougeard, G. *et al.* Molecular basis of the Li-Fraumeni syndrome: an update from the French LFS families. *J Med Genet* **45**, 535-538 (2008).
23. Morton, J.P. *et al.* Mutant p53 drives metastasis and overcomes growth arrest/senescence in pancreatic cancer. *Proc Natl Acad Sci U S A* **107**, 246-251 (2010).
24. Bouaoun, L. *et al.* TP53 Variations in Human Cancers: New Lessons from the IARC TP53 Database and Genomics Data. *Hum Mutat* **37**, 865-876 (2016).
25. Rotter, V. p53, a transformation-related cellular-encoded protein, can be used as a biochemical marker for the detection of primary mouse tumor cells. *Proc Natl Acad Sci U S A* **80**, 2613-2617 (1983).
26. Yemelyanova, A. *et al.* Immunohistochemical staining patterns of p53 can serve as a surrogate marker for TP53 mutations in ovarian carcinoma: an immunohistochemical and nucleotide sequencing analysis. *Mod Pathol* **24**, 1248-1253 (2011).
27. Terzian, T. *et al.* The inherent instability of mutant p53 is alleviated by Mdm2 or p16INK4a loss. *Genes Dev* **22**, 1337-1344 (2008).
28. Eischen, C.M. & Lozano, G. The Mdm network and its regulation of p53 activities: a rheostat of cancer risk. *Hum Mutat* **35**, 728-737 (2014).
29. Haupt, Y., Maya, R., Kazaz, A. & Oren, M. Mdm2 promotes the rapid degradation of p53. *Nature* **387**, 296-299 (1997).
30. Kubbutat, M.H., Jones, S.N. & Vousden, K.H. Regulation of p53 stability by Mdm2. *Nature* **387**, 299-303 (1997).
31. Yen, H.C., Xu, Q., Chou, D.M., Zhao, Z. & Elledge, S.J. Global protein stability profiling in mammalian cells. *Science* **322**, 918-923 (2008).
32. Yu, T. *et al.* Profiling human protein degradome delineates cellular responses to proteasomal inhibition and reveals a feedback mechanism in regulating proteasome homeostasis. *Cell Res* **24**, 1214-1230 (2014).

33. Hart, T. *et al.* High-Resolution CRISPR Screens Reveal Fitness Genes and Genotype-Specific Cancer Liabilities. *Cell* **163**, 1515-1526 (2015).
34. Noordermeer, S.M. *et al.* The shieldin complex mediates 53BP1-dependent DNA repair. *Nature* **560**, 117-121 (2018).
35. Jethwa, A. *et al.* TRRAP is essential for regulating the accumulation of mutant and wild-type p53 in lymphoma. *Blood* **131**, 2789-2802 (2018).
36. Lukashchuk, N. & Vousden, K.H. Ubiquitination and degradation of mutant p53. *Mol Cell Biol* **27**, 8284-8295 (2007).
37. Hart, T. *et al.* Evaluation and Design of Genome-Wide CRISPR/SpCas9 Knockout Screens. *G3 (Bethesda)* **7**, 2719-2727 (2017).
38. Tsherniak, A. *et al.* Defining a Cancer Dependency Map. *Cell* **170**, 564-576 e516 (2017).
39. Redston, M.S. *et al.* p53 mutations in pancreatic carcinoma and evidence of common involvement of homocopolymer tracts in DNA microdeletions. *Cancer Res* **54**, 3025-3033 (1994).
40. Lambert, J.P., Tucholska, M., Go, C., Knight, J.D. & Gingras, A.C. Proximity biotinylation and affinity purification are complementary approaches for the interactome mapping of chromatin-associated protein complexes. *J Proteomics* **118**, 81-94 (2015).
41. Roux, K.J., Kim, D.I. & Burke, B. BioID: a screen for protein-protein interactions. *Curr Protoc Protein Sci* **74**, Unit 19 23 (2013).
42. Kim, D.I. *et al.* An improved smaller biotin ligase for BioID proximity labeling. *Mol Biol Cell* **27**, 1188-1196 (2016).
43. Roux, K.J., Kim, D.I., Raida, M. & Burke, B. A promiscuous biotin ligase fusion protein identifies proximal and interacting proteins in mammalian cells. *J Cell Biol* **196**, 801-810 (2012).
44. Paulsen, R.D. *et al.* A genome-wide siRNA screen reveals diverse cellular processes and pathways that mediate genome stability. *Mol Cell* **35**, 228-239 (2009).
45. Stokes, M.P. *et al.* Profiling of UV-induced ATM/ATR signaling pathways. *Proc Natl Acad Sci U S A* **104**, 19855-19860 (2007).
46. Hurov, K.E., Cotta-Ramusino, C. & Elledge, S.J. A genetic screen identifies the Triple T complex required for DNA damage signaling and ATM and ATR stability. *Genes Dev* **24**, 1939-1950 (2010).
47. Matsuoka, S., Huang, M. & Elledge, S.J. Linkage of ATM to cell cycle regulation by the Chk2 protein kinase. *Science* **282**, 1893-1897 (1998).
48. O'Neil, N.J., Bailey, M.L. & Hieter, P. Synthetic lethality and cancer. *Nat Rev Genet* **18**, 613-623 (2017).

49. Montes de Oca Luna, R., Wagner, D.S. & Lozano, G. Rescue of early embryonic lethality in mdm2-deficient mice by deletion of p53. *Nature* **378**, 203-206 (1995).
50. Mi, H. *et al.* PANTHER version 11: expanded annotation data from Gene Ontology and Reactome pathways, and data analysis tool enhancements. *Nucleic Acids Res* **45**, D183-D189 (2017).
51. Benslimane, Y. *et al.* A novel p53 regulator, C16ORF72/TAPR1, buffers against telomerase inhibition. *Aging Cell* **20**, e13331 (2021).
52. Hustedt, N. *et al.* A consensus set of genetic vulnerabilities to ATR inhibition. *bioRxiv*, 574533 (2019).
53. Amici, D.R. *et al.* Coessential Genetic Networks Reveal the Organization and Constituents of a Dynamic Cellular Stress Response. *bioRxiv*, 847996 (2019).
54. Langille E, A.-Z.K., Ma Z, Malik A, Loganathan S, Treka D, Liu J, Kozma K, Tsai R, Trng K, Espin R, Barutcu S, Ngeuyen T, Bremner R, Jackson H, Knudsen E, Bader G, Egan S, Pujana M, Wrana J, Wahl G, Schramek D Loss of epigenetic regulation disrupts lineage integrity, reactivates multipotency and promotes breast cancer. *bioRxiv 2021; revised and resubmitted to Cancer Discovery*, 2021.2010.2022.465428 (2021).
55. Adams, J.R. *et al.* Cooperation between Pik3ca and p53 mutations in mouse mammary tumor formation. *Cancer Research* **71**, 2706-2717 (2011).
56. Bossi, G. *et al.* Mutant p53 gain of function: reduction of tumor malignancy of human cancer cell lines through abrogation of mutant p53 expression. *Oncogene* **25**, 304-309 (2006).
57. Hui, L., Zheng, Y., Yan, Y., Bargonetti, J. & Foster, D.A. Mutant p53 in MDA-MB-231 breast cancer cells is stabilized by elevated phospholipase D activity and contributes to survival signals generated by phospholipase D. *Oncogene* **25**, 7305-7310 (2006).
58. Alexandrova, E.M. *et al.* Improving survival by exploiting tumour dependence on stabilized mutant p53 for treatment. *Nature* **523**, 352-356 (2015).
59. Sun, L. *et al.* JFK, a Kelch domain-containing F-box protein, links the SCF complex to p53 regulation. *Proc Natl Acad Sci U S A* **106**, 10195-10200 (2009).
60. Sun, L. *et al.* Substrate phosphorylation and feedback regulation in JFK-promoted p53 destabilization. *J Biol Chem* **286**, 4226-4235 (2011).
61. Yue, X. *et al.* BAG2 promotes tumorigenesis through enhancing mutant p53 protein levels and function. *Elife* **4** (2015).
62. Yue, X. *et al.* A novel mutant p53 binding partner BAG5 stabilizes mutant p53 and promotes mutant p53 GOFs in tumorigenesis. *Cell Discov* **2**, 16039 (2016).
63. Zhao, Y. *et al.* Pontin, a new mutant p53-binding protein, promotes gain-of-function of mutant p53. *Cell Death Differ* **22**, 1824-1836 (2015).

64. Shimada, K., Bachman, J.A., Muhlich, J.L. & Mitchison, T.J. shinyDepMap, a tool to identify targetable cancer genes and their functional connections from Cancer Dependency Map data. *Elife* **10** (2021).
65. Garofano, L. *et al.* Pathway-based classification of glioblastoma uncovers a mitochondrial subtype with therapeutic vulnerabilities. *Nat Cancer* **2**, 141-156 (2021).
66. Zhang, D., Zaugg, K., Mak, T.W. & Elledge, S.J. A role for the deubiquitinating enzyme USP28 in control of the DNA-damage response. *Cell* **126**, 529-542 (2006).
67. Cuella-Martin, R. *et al.* 53BP1 Integrates DNA Repair and p53-Dependent Cell Fate Decisions via Distinct Mechanisms. *Mol Cell* **64**, 51-64 (2016).
68. Lambrus, B.G. *et al.* A USP28-53BP1-p53-p21 signaling axis arrests growth after centrosome loss or prolonged mitosis. *J Cell Biol* **214**, 143-153 (2016).
69. Wang, X. *et al.* Targeting deubiquitinase USP28 for cancer therapy. *Cell Death Dis* **9**, 186 (2018).
70. Sanders, S.J. *et al.* Multiple recurrent de novo CNVs, including duplications of the 7q11.23 Williams syndrome region, are strongly associated with autism. *Neuron* **70**, 863-885 (2011).
71. Chang, J.R. *et al.* Role of p53 in neurodegenerative diseases. *Neurodegener Dis* **9**, 68-80 (2012).
72. Wong, S. *et al.* Role of p53, Mitochondrial DNA Deletions, and Paternal Age in Autism: A Case-Control Study. *Pediatrics* **137** (2016).

References for Materials & Methods.

73. Zimmermann, M. *et al.* CRISPR screens identify genomic ribonucleotides as a source of PARP-trapping lesions. *Nature* **559**, 285-289 (2018).
74. Li, W. *et al.* MAGeCK enables robust identification of essential genes from genome-scale CRISPR/Cas9 knockout screens. *Genome Biol* **15**, 554 (2014).
75. Colic, M. *et al.* Identifying chemogenetic interactions from CRISPR screens with drugZ. *Genome Med* **11**, 52 (2019).
76. Coyaud, E. *et al.* BioID-based Identification of Skp Cullin F-box (SCF)beta-TrCP1/2 E3 Ligase Substrates. *Mol Cell Proteomics* **14**, 1781-1795 (2015).
77. Hesketh, G.G., Youn, J.Y., Samavarchi-Tehrani, P., Raught, B. & Gingras, A.C. Parallel Exploration of Interaction Space by BioID and Affinity Purification Coupled to Mass Spectrometry. *Methods Mol Biol* **1550**, 115-136 (2017).
78. Teo, G. *et al.* SAINTq: Scoring protein-protein interactions in affinity purification - mass spectrometry experiments with fragment or peptide intensity data. *Proteomics* **16**, 2238-2245 (2016).

79. Kim, E. & Hart, T. Improved analysis of CRISPR fitness screens and reduced off-target effects with the BAGEL2 gene essentiality classifier. *Genome Med* **13**, 2 (2021).
80. Lamprecht, M.R., Sabatini, D.M. & Carpenter, A.E. CellProfiler: free, versatile software for automated biological image analysis. *Biotechniques* **42**, 71-75 (2007).
81. Lu, Y. *et al.* Interaction of adenovirus type 5 E4orf4 with the nuclear pore subunit Nup205 is required for proper viral gene expression. *J Virol* **88**, 13249-13259 (2014).
82. Xiao, G. *et al.* Gain-of-Function Mutant p53 R273H Interacts with Replicating DNA and PARP1 in Breast Cancer. *Cancer Res* **80**, 394-405 (2020).

Figure Legends

Figure 1. CRISPR screen for regulators of wild-type and mutant p53 stability

(A) Reporter design. Schematic of the fluorescence reporter based on a bicistronic p53-mClover stability sensor followed by a co-translational self-cleaving P2A peptide and mRFP that serves as an internal control. Any perturbation that specifically affects p53 stability would result in an altered mClover/RFP ratio (#1 diagonal axis), while any perturbation that results in overall increased transcription or general differences of proteostasis would affect RFP as well as p53-mClover (#2 horizontal axis).

(B) Flow cytometry blots depicting the level of wild-type and mutant p53 protein reporters upon Nultin-3a (10 uM, 24 hours) treatment to inhibit the interaction between MDM2 and p53 and upon Nultin-3a withdrawal (24 hours).

(C) Flow cytometry blots depicting the levels of wild-type and p53 R273H protein reporters upon CRISPR/Cas9-mediated MDM2 depletion (top), or upon subsequent MDM2 overexpression (bottom), measured 7 days post-transduction.

(D) Schematic of the screening set up and analysis. Each clonal reporter line was transduced with a lentiviral genome-wide CRISPR knockout library (TKOv3). Infected populations were drug selected and sorted by Fluorescence-Activated Cell Sorting (FACS) into mClover-low and mClover-high pools. sgRNA barcodes were amplified and their abundance in each pool was determined by next generation sequencing.

(E, F) Screen results for wild-type and p53 R273H protein reporters. Volcano plots displaying the perturbation effects (log 2-fold change, LFC) of each gene based on two replicates per screen. To compare among different screens (G, H), the perturbation effects of each gene was further normalised as normZ scores, considering both the LFC and false discovery rate (FDR) values. Hits were defined as having $|\text{normZ}| \geq 3$. On the volcano plots, hits satisfying both $\text{FDR} > 0.5$, and $\text{LFC} \geq 1$ (red) or $\text{LFC} \leq -0.8$ (blue), are labelled in red for genes whose losses lead to increased p53 levels and blue for genes whose losses decreased p53.

(G) Unsupervised hierarchy clustering of the wild-type and five screened p53 mutants, using the normalised screening results (normZ) of all 18053 genes.

(H) UpSet plot displaying hits shared amongst each mutant screened. The loss-of-function of an “up” (red) or “down” (blue) hit would result in that p53 mutant to destabilise or stabilise, respectively. Each column indicates a set of wt and/or p53 mutants, and the histogram above indicates the number of genes in this intersecting set; the filled-in cells show which p53 (wt or mutants) is a part of this intersection.

Figure 2. FBXO42-CCDC6 axis regulates mutant p53 protein stability

(A) Heatmap of the essentiality scores of top correlated (positive) and anti-correlated (negative) genes with *FBXO42* across 789 cancer cell lines screened in DepMap (depmap.org, generated using shinyDepMap⁶⁴).

- (B) The 50 top genes correlated (blue) and anti-correlated (red) with *FBXO42*, based on coessentiality results from CRISPR screens in 789 cancer cell lines (depmap.org).
- (C) Heatmap displaying the screening results (as normZ scores) of selected hits across wild-type and five p53 mutants. A positive normZ (red) indicates that genetic ablation of a gene leads to increased p53 protein stability, and negative normZ (blue) indicates decreased p53 stability.
- (D) Flow cytometry blots depicting wild-type and R273H p53-mClover levels upon CRISPR/Cas9-mediated depletion of indicated genes. Independent sgRNAs different from the sgRNAs in the screening library were used (red) and the effects were compared against control guides targeting the AAVS1 safe harbour (blue).
- (E) Representative Western Blot showing p53^{R273H}-mClover protein levels in clonal RPE1 p53 R273H reporter cell line upon clonal depletion of *CCDC6* or *FBXO42*, and upon proteasomal inhibition (10 μ M MG132 for 12 hours). GAPDH serves as a loading control.
- (F) Representative Western Blot showing endogenous p53 R273H protein levels in PANC-1 cells upon depletion of *CCDC6* and *FBXO42*, and upon genotoxic stress (IR 0.5 Gy, 24 hours after). GAPDH serves as a loading control. Bar graph depicts quantification of p53 levels over 3 independent biological replicates (*: $p < 0.05$). Error bar = standard error of the mean (S.E.M.).
- (G) Flow cytometry blots depicting the p53^{R273H}-mClover levels upon depletion of *CCDC6* or *FBXO42*, and upon ectopic re-expression of *CCDC6* or *FBXO42*.
- (H) Flow cytometry blots depicting p53^{R273H}-mClover levels upon depletion of *FBXO42* and ectopic re-expression of Δ Fbox *FBXO42* (lacking aa 44-93) or Δ Kelch *FBXO42* (lacking aa 132-432).

Figure 3. Mapping the genetic interaction network of *FBXO42*-*CCDC6* and mutant p53

- (A) Selected proximity interactors of p53 R273H, *CCDC6* and *FBXO42* as mapped by BioID using HEK293-Flp-In T-REx cell lines stably expressing each bait, with or without the proteasomal inhibitor MG132 [5 μ M, 24 hours]. The spectral count of each prey is depicted by the intensity of the shade filling, the relative abundance of this prey compared across all baits is by the size of the circle, and the confidence (Bonferroni false discovery rate, BFDR) is by the intensity of the edge.
- (B) Interaction of p53 R273H and *CCDC6* in PANC-1 cells validated using immunoprecipitation (IP). Lysates of PANC-1 cells with or without depletion of the endogenous p53 R273H protein were immunoprecipitated using an *CCDC6*-specific antibody or an IgG-isotype control, followed by Western blot analysis of the endogenous p53. β -actin serves as a loading control for lysates input.
- (C) Proximity ligation assay (PLA) between endogenous *CCDC6* and endogenous p53 R273H in PANC-1 cells using tetramethylrhodamine-5-isothiocyanate (TRITC) as a probe (red) and counterstained with DAPI (blue) and phalloidin-FITC (green) to visualise nuclear DNA and F-actin, respectively. RNAi mediated depletion of the the endogenous p53 R273H protein was used as control to show specificity.

(D) *In vitro* binding assay of p53 core domain with FBXO42. The MBP-tagged Kelch domain of FBXO42 (FBXO42c, aa 105-360), and the core DNA-binding domain of p53 R273H (p53-CD-R273H, aa 90-311, untagged) were expressed and purified from bacteria. Untagged p53-CD-R273H does not interact with Amylose resin, while MBP-FBXO42c is pulled down by Amylose. Upon incubation of MBP-FBXO42c and p53-CD-R273H, p53-CD-R273H was found in the pulled down fraction; the input, Amylose-bound and Amylose-unbound fractions were resolved in SDS-PAGE and stained with Coomassie Blue.

(E, F) Scatter plots of the perturbation effect of each gene as normalised Z-score (normZ), in the p53 R273H reporters before and after the loss of *CCDC6* or *FBXO42*. Selected genes whose depletion resulted in p53 stabilisation and destabilisation are marked in red and green, respectively.

(G, H) Representative Western blot results showing levels of USP28 and p53 in nuclear and cytoplasmic fractions of the p53 R273H reporter cell line with clonal depletion of FBXO42 or *CCDC6*, and upon the ectopic re-expression of *CCDC6* or FBXO42. Histone H3 and GAPDH served as nuclear and cytoplasmic markers, respectively. Levels of *CCDC6* and FBXO42 were measured from the total cell lysates (H).

(I) Total cellular USP28 and p53 levels in PANC-1 cells upon depletions of *CCDC6*, *FBXO42*, or *USP28*.

Figure 4. Synthetic viability screen maps regulators of p53.

(A) Pathway analysis based on the top scoring genes from the protein stability reporter screens that resulted in increased wild-type or mutant p53 levels using Reactome pathway analysis. Selected Reactome pathways are shown.

(B) Synthetic viability screen. Bayesian Factors (BF) as a measurement of essentiality (high values indicate a lethal gene) are shown for all protein-coding genes in p53 wild-type versus p53 null background.

(C) Pathway analysis based on the top scoring genes in the synthetic viability screen using Reactome pathway analysis. Selected Reactome pathways are shown.

(D) Venn diagram depicting the top scoring genes from the synthetic viability screen and the top scoring genes from the p53 stability screens whose mutation leads to increased p53 levels. The common genes from both screens are depicted.

(E) Heatmap of the essentiality scores of top correlated (positive) and anti-correlated (negative) genes with *C16orf72* across 789 cancer cell lines screened in DepMap (depmap.org, generated using shinyDepMap⁶⁴).

(F) The 50 top genes correlated (blue) and anti-correlated (red) with *C16orf72*, based on coessentiality results from CRISPR screens in 789 cancer cell lines (depmap.org).

Figure 5. C16orf72 is a regulator of wild-type and mutant p53 stability.

(A) Clonogenic survival assays validating the synthetic viability between *C16orf72* and p53. Assayed 13 days after plating, the surviving fractions of RPE1-hTERT-*TP53*^{+/+} or *TP53*^{-/-} cells transduced with the indicated sgRNAs were normalised to those depleted with the non-targetting control guide. Error bar = standard error of the mean (S.E.M.), n=3, ** p<0.01, *** p<0.001.

- (B) Representative Western Blot results showing p53 and p21 protein levels in RPE1 cells transduced with the indicated sgRNAs. GAPDH serves as a loading control.
- (C) Flow cytometry blots depicting the level of wild-type or p53^{R273H}-mClover protein levels upon depletion of *C16orf72*.
- (D) Interactors of *C16orf72* as mapped by APMS in HEK293-Flp-In T-REx and U2OS-Flp-In T-REx cells stably expressing FLAG-tagged *C16orf72*.
- (E) Representative Western Blot results showing p53 protein levels in response to depletions of *C16orf72* and other known E3 ligases of p53 (*MDM2*, *USP7* and *HUWE1*) using siRNAs.
- (F) Co-immunoprecipitation (co-IP) showing an interaction of *C16orf72* and *USP7*. HEK 293 cells stably transduced with an inducible FLAG-*USP7* or FLAG-empty vector control vector were transfected with either an HA-tagged *C16orf72* or an HA-empty control vector. Lysates with or without doxycycline-induction were co-IPed using a FLAG-specific antibody, followed by Western Blot analysis of HA. GAPDH serves as a loading control for the lysate input.

Figure 6. *C16orf72* functions as oncogene and regulates p53 stability in the mammary gland

- (A) cBioPortal OncoPrint displaying a trend toward mutual exclusivity between genetic ablation of *TP53* and *C16orf72* amplification, and co-amplification between *USP7* and *C16orf72*, among breast cancer patients.
- (B) *In vivo* cell competition assay in the mouse mammary glands. LSL-Cas9-EGFP (*Trp53*^{+/+}) or the LSL-Cas9-EGFP; *Trp53*^{flx/flx} (*Trp53*^{-/-}) mice were intraductally injected with a mixture of control lentiviral particles expressing Cre and BFP as well as an sgRNA targeting the *Tigre* safe harbour, and experimental lentiviral particles expressing Cre and RFP as well as an sgRNA targeting *Tigre*, *C16orf72* or *Mdm2*. The number of surviving cells that had been depleted of each gene were counted 12 days post injection, and normalised to the number of cells depleted of *Tigre* in the same gland. This ratio was further normalised to the ratio of sgTigre:sgTigre in the LSL-Cas9-EGFP; *Trp53*^{flx/flx} mouse. Error bar = standard error of the mean (S.E.M.), n=3 glands, * p<0.05.
- (C) Flow cytometry plot depicting the p53^{R273H}-mClover levels in RPE1 reporter cells upon overexpression of *C16orf72*.
- (D) Western blot analysis of wildtype p53 levels in human MCF10A mammary epithelial cells overexpressing *C16orf72*, assayed after treatment with Doxorubicin [2 µg/mL] for 6 hours.
- (E) Kaplan-Meier plot depicting the tumour-free survival of tumour-prone LSL-*Pi3k*^{H1047R} mice intraductally injected with lentiviral particles expressing Cre as well as *C16orf72*, *Usp7*, *Mdm2*, or control (mRuby). (n=5 for each condition)
- (F) Immunohistochemistry stainings of p53 and GFP in mouse mammary hyperplasia and tumour from mice LSL-*Pi3k*^{H1047R}; LSL-EGFP intraductally injected with lentiviral particles expressing Cre as well as

C16orf72 or control. Stage-matched lesions from LV-C16orf72-Cre or LV-Ruby-Cre transduced LSL-*Pi3k*^{H1047R} glands were stained for p53 and GFP in consecutive sections and counterstained by Hematoxylin. GFP serves as lineage trace to identify transduced cells. Scale bar = 100 um.

Antibody are detailed in **Suppl. Table 7**.

Supplemental figure legends

Figure S1. CRISPR screen for regulators of p53 stability.

(A) Flow cytometry blots depicting the dynamic levels of each p53 mutant after x-irradiation (1 Gy) over time.

(B) Unsupervised hierarchy clustering of each screen replicate (left) and visualised as t-distributed stochastic neighbor embedding (t-SNE) blot (right). The inter-run correlation of each screen is computed by comparing the normZ scores of each gene from the two replicates.

Figure S2. CRISPR screen for regulators of p53 stability.

(A-D) Screen results for R175H, G245, R248Q, and R337H p53 stability reporter screens.

(E) Comparison of different p53 mutants and the effects on their stabilities (normZ scores) upon CRISPR/Cas9-mediated mutagenesis of individual members of the proteasome subunits. A positive normZ (red) indicates that genetic ablation of a gene leads to increased p53 protein stability, and negative normZ (blue) indicates decreased p53 stability.

(F) Guides efficiency measured as genetic indel abundances of sgRNAs targeting *CCDC6*, *FBXO42*, and *MDM2*, in the clonal RPE1-reporters and PANC-1 lines, using Inference of CRISPR Edits (ICE) analysis. The knockout efficiency (indel%) of each guide in the PANC-1-Cas9 line is displayed as a histogram.

Figure S3. FBXO42-CCDC6 axis regulates p53 stabilities across wild-type and different mutants.

(A) Flow cytometry blots depicting the levels of indicated p53 mutants upon depletions of *CCDC6* and *FBXO42* measured 10 days post-transduction.

(B) Flow cytometry blots depicting the levels of p53 R273H mutant upon depletion of *CCDC6* or *FBXO42* and after x-irradiation (0.5 Gy) over time. The percentage of p53-mClover low and high cells is displayed.

(C) Western blot analysis of endogenous p53 R273H protein levels in PANC-1-Cas9 cells upon depletions of *CCDC6* or *FBXO42* measured 10 days post-transduction, and at various time points after irradiation.

(D) Quantification of p53 R273H protein levels in PANC-1-Cas9 cells upon depletions of *CCDC6*, or *FBXO42*, and at various time points after irradiation, measured using flow cytometer at 10 days post-transduction.

The ratios of the bimodal populations (p53-mClover high vs low) from all time points were normalized to the untreated sgAAVS1 control group. (*: $p < 0.08$, error bar indicates standard deviation of the mean).

(E) Flow cytometry blots depicting the p53^{R273H}-mClover levels upon depletion of *CCDC6* or *FBXO42* and treatment with the proteasomal inhibition MG132 (10uM; 12 hours).

(F) Quantitative real-time PCR analysis of the PANC-1 cells with depletion of *CCDC6* or *FBXO42*. The *TP53* transcript level was normalised to the house keeping gene Peptidyl-prolyl cis-trans isomerase B (*PPIB*). Experiment performed in biological triplicates.

(G) Western blot showing the expression levels of the FBXO42 full length protein and the indicated FBXO42 truncation mutants.

(H) Schematic of FBXO42 and its functional domains. The Kelch domain AA numbers correspond to those removed from each subsequent truncation mutant in (I).

(I) Flow cytometry blots depicting the p53^{R273H}-mClover levels upon depletion of *FBXO42* and ectopic expression of various FBXO42 truncation mutants measured at 7 days post-transduction. The truncation domains are illustrated by the schematics in (H).

Figure S4. Mapping the genetic interaction network of FBXO42-CCDC6 and mutant p53.

(A) Co-immunoprecipitation (co-IP) showing interaction of CCDC6 and p53 R273H in PANC-1 cells. Lysates of PANC-1 cells overexpressing V5-tagged CCDC6 or a GFP control construct with or without genetic ablation of the endogenous p53 R273H gene were immunoprecipitated using an V5-specific antibody, followed by Western blot analysis of endogenous p53.

(B) Flow cytometry blots depicting the p53^{R273H}-mClover levels upon depletion of *CCDC6* or *FBXO42* or *USP28* or upon concomitant depletion of *USP28* and *CCDC6* or concomitant depletion of *USP28* and *FBXO42*.

(C) Immunofluorescence imaging showing localization and levels of R273H p53-mClover (FITC) and USP28 (Alexa 568) in RPE1 p53^{R273H}-mClover cells with depletion of *CCDC6* or *FBXO42*. The ratio of cytoplasmic to nuclear intensities were quantified (n>200). Error bar = S.E.M. *** p<0.01.

(D) Quantitative real-time PCR analysis of the PANC-1 cells with depletion of *CCDC6* or *FBXO42*. The *USP28* transcript level was normalised to *PPIB*. Experiment performed in biological triplicates.

(E) Flow cytometry blots depicting p53^{R273H}-mClover levels in p53 R273H-reporter RPE1 cells with clonal depletions of *USP28* (left), *FBXO42* (middle) or *CCDC6* (right), upon ectopic expression of CCDC6 FBXO42 or USP28, measured at 7 days post-transduction.

Figure S5. C16orf72 functions as oncogene and regulates p53 stability in the mammary gland

(A) Flow cytometry blots depicting the levels of p53 G245S, R248Q, and R248W in the p53-mClover RPE1 reporter cells upon depletion of *C16orf72*.

(B) cBioPortal OncoPrint displaying mutations, amplifications, deletions and structural variants of *C16orf72* in all cancers.

(C) cBioPortal OncoPrint displaying amplifications and gains of *C16orf72* in all cancers.

(D) Kaplan-Meier plot comparing the tumour-free survival of tumour-prone LSL-*Pi3k*^{H1047R} mice intraductally injected with lentiviral particles expressing Cre as well as a sgRNA targeting Trp53 (sgTrp53-Cre) or the control safe harbor locus Tigre (sgTigre-Cre). (n=5 for each condition.)

Supplementary Table Legends

Supplementary Table 1. p53 stability screening results

Sheet 1 lists NormZ and FDR values of all the genes and all p53 stability reporters.

Sheet 2 lists LFC and FDR values of all the genes and all p53 stability reporters.

Sheet 3 lists all gene hits.

Supplementary Table 2. p53, FBXO42, CCDC6 BioID results

List of all proximity interactors and their spectral counts for CCDC6, FBXO42 and p53 R273 with or without MG132 treatment.

Supplementary Table 3. ReactomePathway analysis of p53 Destabilizers

Sheet 1 lists all significantly dysregulated pathways obtained from a ReactomePathway analysis of p53 destabilizers.

Sheet 2 lists selected dysregulated pathways obtained from a ReactomePathway analysis of p53 destabilizers used for Fig. 4a.

Supplementary Table 4. Results of Synthetic Viability screen

Sheet 1 lists Bayes Factors for all genes in p53 proficient and p53 deficient RPE1 cells from the Synthetic Viability screens.

Sheet 2 lists Bayes Factors for hits identified from the Synthetic Viability screens.

Supplementary Table 5. ReactomePathway analysis of Synthetic Viability screen

List of all significantly dysregulated pathways obtained from a ReactomePathway analysis of the Synthetic Viability screen as well as selected dysregulated pathways used for Fig. 4c.

Supplementary Table 6. C16orf72 APMS-SAINTE results

Sheet 1 lists all proteins identified in the C16orf72 AP-MS experiment and their spectral counts in HEK293T cells.

Sheet 2 lists all proteins identified in the C16orf72 AP-MS experiment and their spectral counts in U2OS cells.

Supplementary Table 7. List of primers, antibodies, sgRNAs

List of the antibodies, order number, supplier and concentrations used in the study.

Materials & Methods

Materials Availability

DNA constructs and other research reagents generated by the authors will be distributed upon request to other academic research investigators under a Material Transfer Agreement. In addition, DNA constructs will also be deposited to Addgene.

Cell lines

RPE1-hTERT (ATCC CRL-4000) and PANC-1 (ATCC CRL-1469) cell lines were maintained in Dulbecco's modified Eagle's medium (DMEM; Wisent Inc.), supplemented with 10% (vol/vol) fetal bovine serum (Wisent Inc.), 100 U/ml of penicillin, and 100 mg/ml of streptomycin (Wisent Inc.) at 37°C under 5% CO₂.

To generate RPE1-based clonal stability reporters, RPE1-hTERT-Cas9-TP53-KO cells⁷³ were transduced with recombinant pLKO.1-based lentiviruses carrying the p53mClover-P2A-mRFP1 cassette at 0.1 MOI, and single clones selected. The pLKO.1-based p53mClover-P2A-mRFP1 cassette carrying control (no p53), wild-type, or hotspot mutant p53s was generated by restriction enzyme cloning, where all hotspot mutants were first generated using site-directed mutagenesis in the pDONR223 entry clone vector and then sub-cloned into the cassette.

To further generate clonal reporters depleted of hit genes, the RPE1-based reporter was transfected with CRISPR ribonucleoprotein (RNP) complexes containing Cas9 and guides against the gene-of-interests. Clonal lines were selected and verified for homozygous deletions by both PCR-based Inference of CRISPR Edits (ICE) and Western blotting.

To generate other cell lines stably expressing Cas9, each line was transduced with lentiviruses expressing lentiCas9-Blast (Addgene #52962) and selected by Blasticidin to generate either single or clonal lines as specified.

CRISPR and FACS based screens

Stability reporters [150 million (M) cells total] cultured on 15 cm dishes (3 M/plate) were first transduced with the lentivirus-based Toronto Knockout v3 library (TKOv3)³⁷ at a low MOI (~0.30). They were then puromycin-selected [17 µg/mL] for two days for transductants starting at 24th hour-post-transduction (hpt). At 48 hpt, cells were trypsinized and replated back to the same plates while maintaining puromycin-selection. At 72 hpt (time point T0), remaining cells were pooled together, counted to confirm MOI, and divided into two technical replicates (referred to as p53.1 and p53.2 in figures) for subculturing; 30 M cells were further collected to confirm the library gRNA abundance at T0. The subcultured replicates were further maintained in puromycin-free media and passaged every three days (T3 and T6).

10 dpt (T7), all cells were harvested by trypsinization and subjected to live sorting by Fluorescence-Activated Cell Sorting (FACS). Harvested cells were resuspended in FACS sorting buffer (Hanks Balanced Salt Solution, 25 mM HEPES pH 7.0, 2 mM EDTA, 1% Fetal Bovine Serum) at a concentration of 5 M cells per mL and were filtered by 40 μ m nylon mesh to eliminate large aggregates. All cells were then live-sorted (MoFlo Astrios EQ cell sorter, Beckman Coulter) based on both the mClover and mRFP1 signals, where only populations with medium-mRFP1 signals were collected to eliminate populations with large gene-expression changes. For mutants displaying bi-modal-mClover populations, all cells from the mClover-low and mClover-high populations were each collected; for uni-modal mutants, cells with mClover intensity within the highest and lowest 15% populations were each collected. (Fig. 1d) Both technical duplicates were independently sorted and collectively maintained the 200X coverage.

Upon sorting, gDNA from cell pellets was isolated using Wizard Genomic DNA Purification Kit (Promega, Cat# A1120); genome-integrated sgRNA sequences were then amplified by PCR using Q5 Mastermix Next Ultra II (New England Biolabs, Cat# M5044L), with primers v2.1-F1-5' GAGGGCCTATTTCCCATGATTC 3' and v2.1-R1-5' GTTGCGAAAAAGAACGTTACGG 3', followed by a second round of PCR reaction containing i5 and i7 multiplexing barcodes. Final PCR products were gel-purified and sequenced on Illumina NextSeq500 systems to determine sgRNA representation in each sample. The abundance of each guide (guides count) was then analysed by MAGeCK count function with default settings⁷⁴.

To generate the log-fold-change (LFC) rank of each gene, the guides counts from both the p53-low and p53-high populations were processed and compared with the MAGeCK test function with default settings⁷⁴, and the LFC (p53-high vs p53-low) and padj values were computed.

To generate the normZ scores for normalising the LFCs across all screens, the guides counts from both the p53-low and p53-high populations were then analysed by the DrugZ programme with default settings⁷⁵. The normZ and padj values were computed. In this study, a hit was defined as having a |normZ| > 3 and padj < 0.5.

All flowcytometry was performed on Fortessa X20 (BD), and data was analysed using the FlowJo software (BD).

Plasmids, transfection and transduction

To generate the lentiviral plasmids for transducing the reporter lines, the reporter plasmid was first built upon the pLKO.1 - TRC cloning vector (Addgene #10878), by substituting the Puromycin resistance gene with the p53mClover2-P2A-mRFP1 or mClover2-P2A-mRFP1 (empty control) cassette. All hotspot mutants were first generated using site-directed mutagenesis in the pDONR223 entry clone vector and then sub-cloned into the cassette by substituting the relevant regions of WTp53. All constructs were confirmed by DNA sequencing. To generate V5-tagged lentiviral overexpression constructs, each open reading frame (ORF) was first generated as an entry clone into the pDONR223 vector using the BP recombination

reaction, and then was cloned into the pLEX_306 expression vector (Addgene #41391) using the LR recombination reaction, following manufacturer's instruction (Invitrogen). Lastly, HA-C16orf72 was generated in the pCDNA3.1-HA backbone, and the FLAG-USP7 was a generous gift of Lori Frappier (University of Toronto).

To generate the entry clone for each of the p53 mutants, the coding sequence of WT p53 (NM_000546.6:143-1324) was first cloned into the pDONR223 vector, retaining Start codon (ATG) and removing the Stop codon (TGA), using the BP recombination reaction (Invitrogen). Each mutant was then generated using PCR-based site-directed mutagenesis to generate p53^{mutant}-pDONR223, with specific codon and primers detailed in Suppl. Table 7. All constructs were sequence verified by Sanger sequencing covering the entire ORF.

For *in vivo* overexpression assays, the pLEX_306-ORF-Cre backbone was first generated by modifying the pLEX_306 by substituting the Puromycin resistance cassette with NLS-iCre. ORFs were then introduced by pDONR223-based entry clone similar to the V5-tagged constructs above. For *in vivo* competition assays, pLKO-H2BFP-P2A-NLSiCre was first generated by replacing the NLSiCre with the H2BFP-P2A-NLSiCre cassette in the pLKO-Cre stuffer v4 (Addgene #158032) backbone; the XFP used was mRFP1 or TagBFP. The guides targeting the each desired gene was then cloned into the vector and sequence confirmed.

For transfections, cells were grown in 100-mm (for immunoprecipitation) dishes to about 70% confluence and transfected with Lipofectamine 3000 (Invitrogen) according to the manufacturer's protocols.

For all lentiviral transduction for *in vitro* (cultured cells) experiments, lentiviral particles were first produced in the 293 TN cells (Systembio LV900A-1), by co-transfecting the lentiviral plasmid with helper plasmids pMD2.G and psPAX2. Supernatant was then harvested at 48 hours post-transfection, and used to transduce cells at an MOI of ~0.1 to 0.3.

For all *in vivo* lentiviral transductions, lentiviral particles were first produced similar to those for *in vitro* experiment, and followed by concentration of the viruses. In brief, the produced supernatant was first filtered through a Stericup-HV PVDF 0.45 µm filter, and then concentrated by ~1000 fold by ultracentrifugation (Beckman Coulter). The titre was quantified by FACS of LSL-tdTomato mouse embryonic fibroblasts (MEFs).

sgRNA sequences for validation experiments from screen hits are detailed in **Suppl. Table 7**.

Analysis of genome editing efficiency

PANC-1 Cas9 cells (for human guides) or LSL-Cas9-EGFP MEFs (for mouse guides) were cultured and transduced with sgRNAs-expressing lentivirus that carries either Puro (for PANC-1) or NLSiCre (for MEFs), carrying each guide. For PANC-1 cells, transduced cells were first selected under Puromycin (5.0 µg/mL) for 48 hours, and then cultured in complete media with passaging every three days until harvesting

on day 10 post-transduction. For MEFs, cells were live sorted for GFP expression and expanded further until harvesting on day 20 post-transduction. At the time of harvesting, the cells were collected by trypsinisation and extracted genomic DNA using DNeasy Blood & Tissue Kit (Qiagen). The genomic region centred at the sgRNA cutting site, along with >250 bps flanking it on each side was PCR amplified, for both cells transduced with guides targeting the desired genes or the control [sgAAVS1 (human) or sgTigre (mouse)]; they were then subject to Sanger sequencing. The editing efficiency was then determined by analysing the sequencing chromatograms with the web-based Interference of CRISPR Edits (ICE) tool, <https://www.synthego.com/products/bioinformatics/crispr-analysis>. Primers for ICE analysis are detailed in **Suppl. Table 7**.

Irradiation and chemical perturbations

RPE1 reporters were treated with ionising radiation (IR) with indicated dose using a Faxitron X-ray cabinet (Faxitron, Tucson, AZ, USA). Chemical perturbation was performed by adding either nutlin 3a (10 nM, Sigma SML0580) or equal volume of DMSO to the complete media. For MG132 treatment of the reporters, either MG 132 (10 μ M, Sigma) or DMSO was added to the complete media for indicated times.

BioID and Affinity Purification Mass Spectrometry (APMS)

BioID group (p53 R273H, CCDC6 and FBXO42). BioID was carried out, essentially as previously described^{43, 76, 77}. In brief, 293 Flp-In T-REx (Invitrogen) cells inducibly expressing C-terminally-tagged full length human p53R273H, CCDC6 and FBXO42 or controls (GFP in lieu of ORF, and vector control alone) were first generated, and inducible expression tested by immunoblotting. Sub-confluent (60%) cells (10 \times 15 cm plates) were incubated for 24 hours in complete media supplemented with 1 μ g/ml tetracycline (Sigma) prior to incubation with 50 μ M biotin (BioShop, Burlington, ON, Canada), and either 5 μ M MG132 (5 plates; calpain inhibitor IV, Z-Leu-Leu-Leu-CHO; American Peptide Company, Sunnyvale, CA) or DMSO (5 plates) for 24 hours. Cells were then collected by first washing twice with PBS and then pelleted (500 g, 5 min), and dried pellets were finally snap frozen.

Affinity purification (BioID group). Cell pellets corresponding to each 15 cm plate were incubated at 4 $^{\circ}$ C in 1:10 (w/v) modified-RIPA buffer (50 mM Tris-HCl pH 7.5, 150 mM NaCl, 1% TritonX-100, 1.5 mM MgCl₂, 1 mM EGTA, 0.1%SDS, Sigma protease inhibitors P8340 1:500, and 0.5% Sodium deoxycholate), and 1 μ L of benzonase (250U) was added to each sample, for 30 min on a rotator. The lysates were then sonicated trice on ice at 35% amplitude. These lysates were then centrifuged and supernatant proceeded for streptavidin-sepharose beads (GE Cat# 17-5113-01) affinity purification, which was performed at 4 $^{\circ}$ C on a rotator for 3 hours, followed by washing the beads once with 2% SDS buffer, twice with modified-RIPA buffer and lastly once in TAP lysis buffer (50mM HEPES-KOH pH 8.0, 100mM

KCl, 2mM EDTA, 0.1% NP-40). Finally, the beads were washed in the ABC buffer (50mM ammonium bicarbonate, pH 8.3) and proteins digested on beads with TPCK-trypsin (Promega, Madison, WI, 16 hours at 37 °C). The supernatant containing the tryptic peptides was collected and lyophilized. Peptides were resuspended in 0.1% formic acid and analyzed by mass spectrometry.

APMS group (C16orf72). Similarly, 293 Flp-In T-REx (Invitrogen) cells inducibly expressing N-terminally-tagged full length human C16orf72 or GFP-control were generated and inducible expression tested by immunoblotting. Sub-confluent (60%) cells (2 × 15 cm plates) were incubated for 24 hours in complete media supplemented with 1 µg/ml tetracycline (Sigma) prior to harvesting similar to the BioID group.

Affinity purification (APMS group). Cell pellets corresponding to 2 × 15 cm plate were incubated at 4 °C in 1:4 (w/v) FLAG-IP lysis buffer (50 mM HEPES pH 8.0, 100 mM KCl, 2 mM EDTA, 0.1% NP40, 10% glycerol, 1 mM PMSE, 1 mM DTT, and Sigma protease inhibitors P8340 1:500). Resuspended lysates were first froze and thawed twice (dry ice and 37 °C waterbath) for 5-10 minutes each. They were then sonicated for 20 seconds at 35% amplitude. 200 units of benzonase was then added to the sample and incubated at 4 °C on a rotator for 20 minutes, and centrifuged to collect the supernatant (16000 g, 20 min, 4 °C). The supernatant were then incubated with magnetic anti-FLAG M2 beads (Sigma, # M8823) at 4 °C on a rotator for 2 hours, at a ratio of 25 µL 50% slurry beads for each IP of 2 × 15 cm plates. Beads were then pelleted by centrifugation (500 g, 5 min), followed by three washes with 1 mL FLAG-IP lysis buffer and two washes with washing buffer (20 mL Tris-HCl pH 8.0 and 2 mM CaCl₂) using a magnetic stand. The samples were then processed similar to the BioID group for on-beads digest and mass spectrometry analysis.

Mass Spectrometry and Data Analysis. Mass spectrometry analysis was carried out as previously described⁷⁷ using the TripleTOF 6600 system (SCIEX). In brief, samples were loaded to fused silica capillary columns pre-loaded with C18 reversed phase material. Ionised peptides were emitted by nanoelectrospray ion source followed by a nano-HPLC system, and analysed using Data Independent Acquisition (DIA) methods.

Interactor Classification. Mass spectrometry data were thresholded for minimum unique spectral count of 2. For APMS group, results from a biological triplicates of the C16orf72 and control were further filtered via significance analysis of interactome (SAINT)⁷⁸, which uses a probability model to assign a confidence score to each interaction by comparing the spectral counts in the sample and control across replicates, thresholded at ProteinProphet p value >0.95 and SAINT BFDR score ≤0.01.

Synthetic lethal screen

It was carried out following previously optimised protocols³³. In brief, isogenic pairs of RPE1-hTERT-Cas9 cells with *TP53*^{+/+} and *TP53*^{-/-} background were each infected with the TKOv3 pooled gRNA library at an MOI of ~0.3. Similar to the stability screen, the infected pools were then selected with puromycin (17

µg/ml, 48 hrs) and maintained in culture for 18 days after Day 0, with passaging of every three days. The genomic DNA from the first and the last timepoint was extracted, and the incorporated gRNA sequences were amplified via 2-step polymerase chain reaction (PCR). The amplification products from the first and the last timepoint were subjected to the Illumina sequencing in order to analyze the fold change of gRNA sequence in cell population.

Data was analyzed with BAGEL2⁷⁹, where positive Bayes factors (BF) values identify genes that are likely essential for proliferation. Hits are defined as concurrently fulfilling $BF > 15$ for *TP53*^{+/+} and $BF < 5$ for *TP53*^{-/-}.

Fluorescence microscopy

Cells were cultured on glass coverslips in 6-well plates for 48 hours (reaching 70% confluency) before fixation with 3.2% paraformaldehyde for 20 minutes, followed by permeabilisation (0.25% v/v Triton-X 100 in 1× Phosphate Buffer Salin (PBS) and blocking (1% w/v BSA, 1% w/v gelatin, 0.25% v/v goat serum, 0.25% v/v donkey serum, 0.25% v/v Triton-X 100 in PBS, in 1× PBS). Samples were then stained for respective antibodies diluted in the blocking buffer for 1 hour at room temperature, followed by washing and staining with secondary antibodies. Coverslips were lastly counterstained with DAPI (4',6-diamidino-2-phenylindole) and mounted on slides using DABCO (Sigma). Cells were then viewed using a Nikon Ti2-E/A1R-Multiphoton microscope equipped with DS-Qi2 camera (Nikon).

For quantification, laser power and gain for each channel and antibody combination were set using secondary only control and confirmation with primary positive control and applied to all images. Images were analysed using Cellprofiler⁸⁰ with default settings to quantify the cytoplasmic to nuclear intensity ratios. The following antibodies were used for IF: p53 (DO-7 FITC conjugate, BD biosciences), USP28 (Bethyl A300-898A), and F-Actin (phalloidin-FITC, Sigma P5282).

Histology and Immunohistochemistry

Tumours or gland tissues were harvested from each endpoint mouse, and placed in 4% PFA for 48 hours. They were then placed into 70% ethanol at stored at 4 °C until standard embedding and sectioning procedure. For staining, the dissected serial section slides were heated at 60 °C for 15 min, then dewaxed and rehydrated. Slides for immunohistochemistry were treated with 3% hydrogen peroxide in PBS for 15 min to deactivate endogenous peroxidases. Slides were then washed in PBS followed by microwave antigen retrieval using Na citrate pH 6.0. Following the primary antibody (diluted in Na citrate solution) incubation at room temperature for 45 min, anti-rabbit secondary antibodies (Vector Labs BA-1000, 1:500 diluted in 0.2% v/v Triton X-100 in PBS) were applied for 35 min at room temperature. This was further followed by ABC kit (Vector Labs PK-4100) treatment for 25 min, and finally DAB Reagent (Vector Labs SK-4100) treatment for 4 min at room temperature. Slides were lastly counterstained for 8 min in Harris Hematoxylin,

dehydrated, and mounted in a xylene based mounting medium. Stained sections were digitized at 40x using a Hamamatsu Nanozoomer Scanner (2.0-HT).

The following primary antibodies were used in this study: anti-p53 rabbit polyclonal antibody (Abcam ab241566, POE316A), anti-GFP rabbit polyclonal antibody (Abcam ab290). Antibody are detailed in **Suppl. Table 7**.

RNA isolation, cDNA synthesis, and real-time QPCR analysis

Total RNAs from PANC-1 cells were first collected using TRIzol (Ambion), treated with ezDNase (Invitrogen), and reverse transcribed into cDNA using SuperScript IV VILO (Invitrogen). Real-time quantitative PCR (qRT-PCR) reactions were performed on an CFX384 (Biorad) in 384-well plates containing 12.5 ng cDNA, 150 nM of each primer, and 5 μ l PowerUp SYBR Green Master Mix (Applied Biosystems) in a 10 μ L total volume. All primers were designed to span exon junctions using Primer3Plus and were melting-curve validated. Relative mRNA levels from experimental triplicates were calculated using the comparative Ct method normalised to *PPIB* mRNA.

With the normalised mRNA levels of targeted genes in the sgAAVS1 sample arbitrarily set as 1.00, the normalised mRNAs in other samples were expressed as a ratio relative to that of sgAAVS1. Statistical significance were determined at $p = 0.05$. Primers for qPCR are detailed in **Suppl. Table 7**.

Immunoprecipitation and Western blotting

Cell extraction and immunoprecipitation were performed as previously described⁸¹. In brief, whole-cell extracts were prepared by lysing cells in buffer X (50 mM Tris pH 8.5, 250 mM NaCl, 1 mM EDTA, 1% NP-40, protease inhibitor minitab (Roche)) and quantified using Bradford assay (Bio-Rad). Equal amounts of protein (lysate or immunoprecipitation samples) were separated by SDS-PAGE and transferred to 0.45 μ m Polyvinylidene fluoride (PVDF) membranes (Immobilon-P, EMD Millipore). For affinity purification of endogenous or epitope-tagged binding proteins, the lysates were incubated with anti-CCDC6 mouse monoclonal antibody (Santa Cruz Q-23) or mouse IgG (Abcam, ab124055), anti-V5 mouse monoclonal antibody (Roche R960-25), or anti-FLAG mouse monoclonal antibody (Sigma M2), followed by protein G beads (Sigma).

For Western blotting, the following antibodies were used for Western blot: p53 HRP-conjugated antibody (R & D Systems, HAF1355), p53 rabbit polyclonal antibody (Santa Cruz FL-393), CCDC6 (Santa Cruz Q-23), FBXO42 (Santa Cruz FL-6), GAPDH HRP-conjugated antibody (BioLegend W17079A), TP53BP1 (BD Biosciences 612523 Clone 19), USP28 (Bethyl A300-898A), USP7 (Bethyl A300-034A), HUWE1 (Abcam ab70161), V5 (Roche R960-25), FLAG (Sigma M2 F7425), HA (Covance HA.11 MMS-101R), and C16orf72 (rabbit polyclonal, in house). Membranes were incubated with primary antibodies followed by appropriate horseradish peroxidase-coupled secondary antibodies (anti-rabbit or anti-mouse

from Jackson ImmunoResearch or TrueBlot anti-mouse from eBioscience). Western Lightning Plus enhanced chemiluminescence substrate (PerkinElmer) was used to visualise proteins on ChemiDoc MP Imager with Image Lab 4.1 software (Bio-Rad) or autoradiography film.

Antibody are detailed in **Suppl. Table 7**.

Nuclear cytoplasmic fractionation

The fractionation was performed using NE-PER Nuclear and Cytoplasmic Extraction Reagents (ThermoFisher) as manufacture instruction. 10 µg of each fraction was separated by SDS-PAGE and transferred to 0.45 µm Polyvinylidene fluoride (PVDF) membranes (Immobilon-P, EMD Millipore).

Clonogenic survival assays

RPE1 cells depleted of each gene using each indicated guide were seeded in 6-well plates (250 cells per well) and cultured using complete media. After 14 days, colonies were stained with crystal violet solution (0.4% w/v crystal violet, 20% methanol), scanned and manually counted. Relative survival was calculated by arbitrarily setting the number of colonies in the Scrambled control as 100%. Experiments were performed in biological triplicates, and the error bar represents the standard error of the mean.

***In situ* proximity ligation assay**

PLA was performed as previously described. In brief, cells were first fixed with 4% PFA for 15 min and permeabilised with 0.1% v/v Triton for 5 min. PLA was performed using the DuoLink *In Situ* PLA Detection Kit (DUO92101, Sigma). Imaging was performed using an LSM 800 (Zeiss) confocal microscope with 40/60 × objective oil immersion.

Protein purification and *in vitro* binding assay

Protein purification was performed as previously described⁸². In brief, the core domain p53 R273H [p53 CD (90-311)] and the Kelch domain of FBXO42 fused with the MBP tag [MBP-FBXO42c (105-360)] were expressed using recombinant expression in *E. coli* B121DE3 cells, followed by cell lysis, Amylose resin, His-Trap chromatography, and size exclusion chromatography (Superdex 75/200). The monomer at >90% purity, with yields of 3-10 mg/L of each protein was obtained and proceeded with binding assays and biophysical characterisation as indicated.

Mice

Animal husbandry, ethical handling of mice and all animal work were carried out according to guidelines approved by Canadian Council on Animal Care and under protocols approved by the Centre for Phenogenomics Animal Care Committee (18-0272H). The parental animals used in this study were Rosa26-LSL-Pik3caH1047R/+ [Gt(ROSA)26Sortm1(Pik3ca*H1047R)Egan] in a pure FVBN background, a

generous gift of Sean Egan, The Hospital for Sick Children/SickKids], Rosa26-LSL-Cas9-GFP (Jackson laboratories #026175, in C57/B16 background), and p53 flox/flox (B6;129S4-Trp53tm5Tyj/J, Jackson laboratories #008361 in B16 background]. Homozygous [p53 flox/flox; Rosa26-LSL-Cas9 GFP], [LSL-Pik3caH1047R], and [p53 flox/flox; LSL-Pik3caH1047R] were each generated by crossing the respective parental lines.

***In vivo* competition and overexpression**

Mice were intraductally injected with lentiviral particles containing either (1) sgRNAs (competition assay) in the #3 or 4 mammary glands with triplicates spreaded across a minimum of two mice (i.e. no more than two glands per mouse containing the same virus), or (2) ORFs (tumour-free survival assay) in both #3 and #4 glands (a total of four per mouse) with five mice per ORF.

Tumour free survival. Mice were monitored weekly (initial three weeks) and then twice-weekly for tumour formation by palpation, and the first appearance of tumours in any gland of the mouse was noted. Mice were harvested when tumours associated with any one gland had reached the tumour burden threshold as defined by the animal ethic guidelines.

Competition. Mice were intraductally injected with a mixture of control lentiviral particles expressing Cre and BFP as well as an sgRNA targeting the *Tigre* safe harbour, and experimental lentiviral particles expressing Cre and RFP as well as an sgRNA targeting *Tigre*, *C16orf72* or *Mdm2*. The number of surviving cells that had been depleted of each gene were counted 12 days post injection, and normalised to the number of cells depleted of *Tigre* in the same gland. This ratio was further normalised to the ratio of sgTigre:sgTigre in the LSL-Cas9-EGFP; *Trp53*^{flox/flox} mouse.

Mammary gland isolation and flowcytometry for lineage tracing. For competition assays, individual mammary glands were harvested digested according to Stemcell Technologies gentle collagenase/hyaluronidase protocol. In brief, glands were first digested overnight (~16 hours) with gentle agitation at 37 °C in 250 µL Gentle Collagenase (Stemcell Technologies #07919) diluted in 2.25 mL of complete Basal Epicult media formulated according to manufacture instructions (Epicult Basal Medium Stemcell Technologies #05610, 10% Proliferation Supplement, 5% v/v FBS, 1% v/v Penicillin-Streptomycin, 10 ng/mL EGF, 10 ng/mL bFGF, 0.0004% v/v heparin). The digested glands were then processed by treating with ammonium chloride and triturated for 2 minutes in pre-warmed trypsin followed by dispase. Cells were stained with CD45, CD31, Ter119, CD49f and EPCAM for luminal and basal cell identification, and Sytox Red for dead cells exclusion. The following antibodies were used for flowcytometry experiment: APC conjugated antiCD45 (Clone 30 F11, BioLegend), APC conjugated antiCD31 (Clone MEC133, BioLegend), APC antiMouse Ter119 (Clone TER-119, BioLegend), PECy7

anti human/mouse CD49f (Clone GoH3, BioLegend), APCVio770 mouse anti-CD326 EpCAM (Clone caa7-9G8, Miltenyi).

Statistics and reproducibility

Unless specified, independent biological replicates were performed, and group comparisons were done as indicated in the legends. $P < 0.05$ was considered significant. Statistical analysis was performed using GraphPad Prism 7. Unless specified, quantitative data are expressed as the mean \pm SE. Differences between groups were calculated by two-tailed Student's t-test, Wilcoxon Rank-Sum test (normal distribution correction) or Log-rank test using Prism 7.

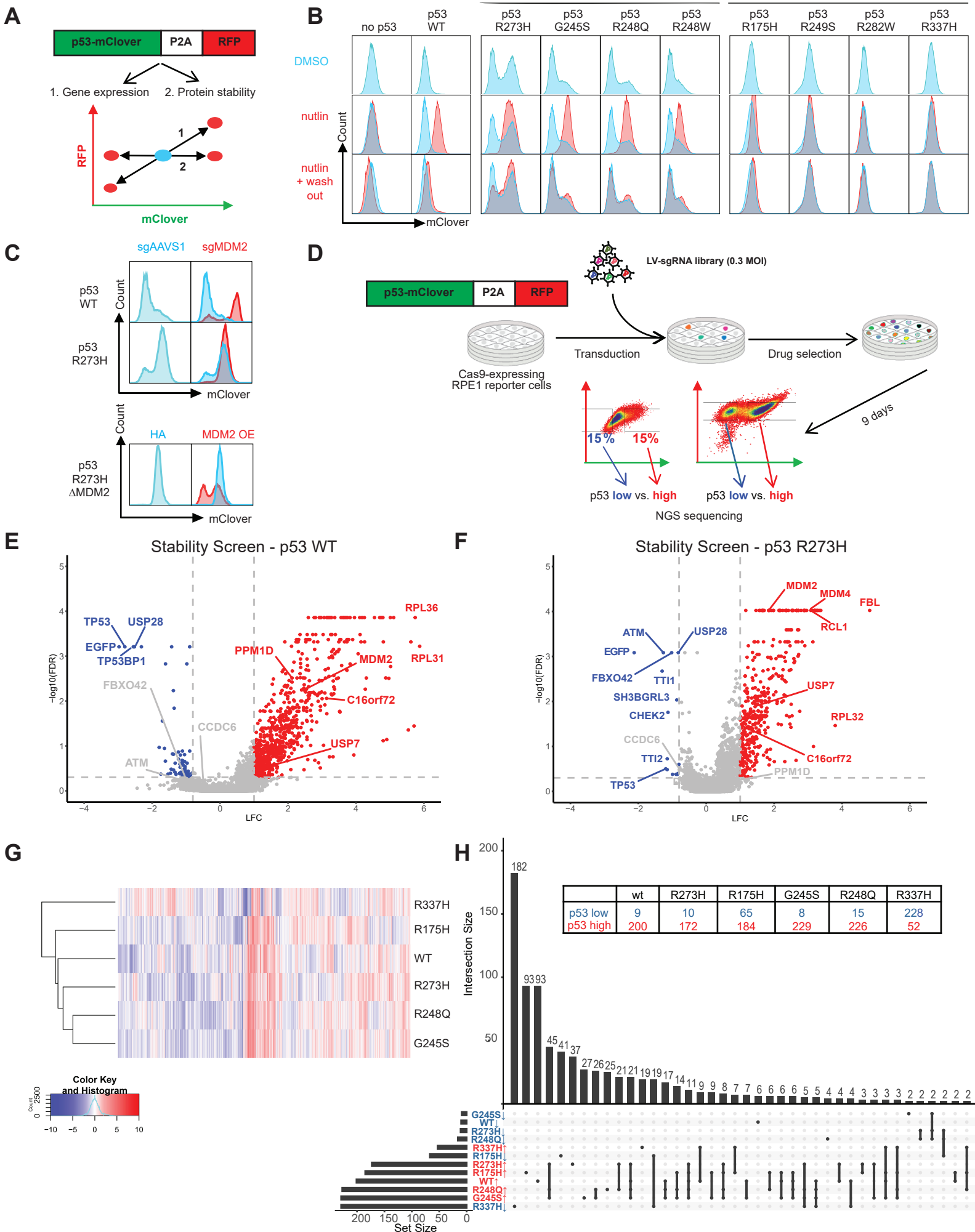


Figure 1. CRISPR screen for regulators of p53 stability

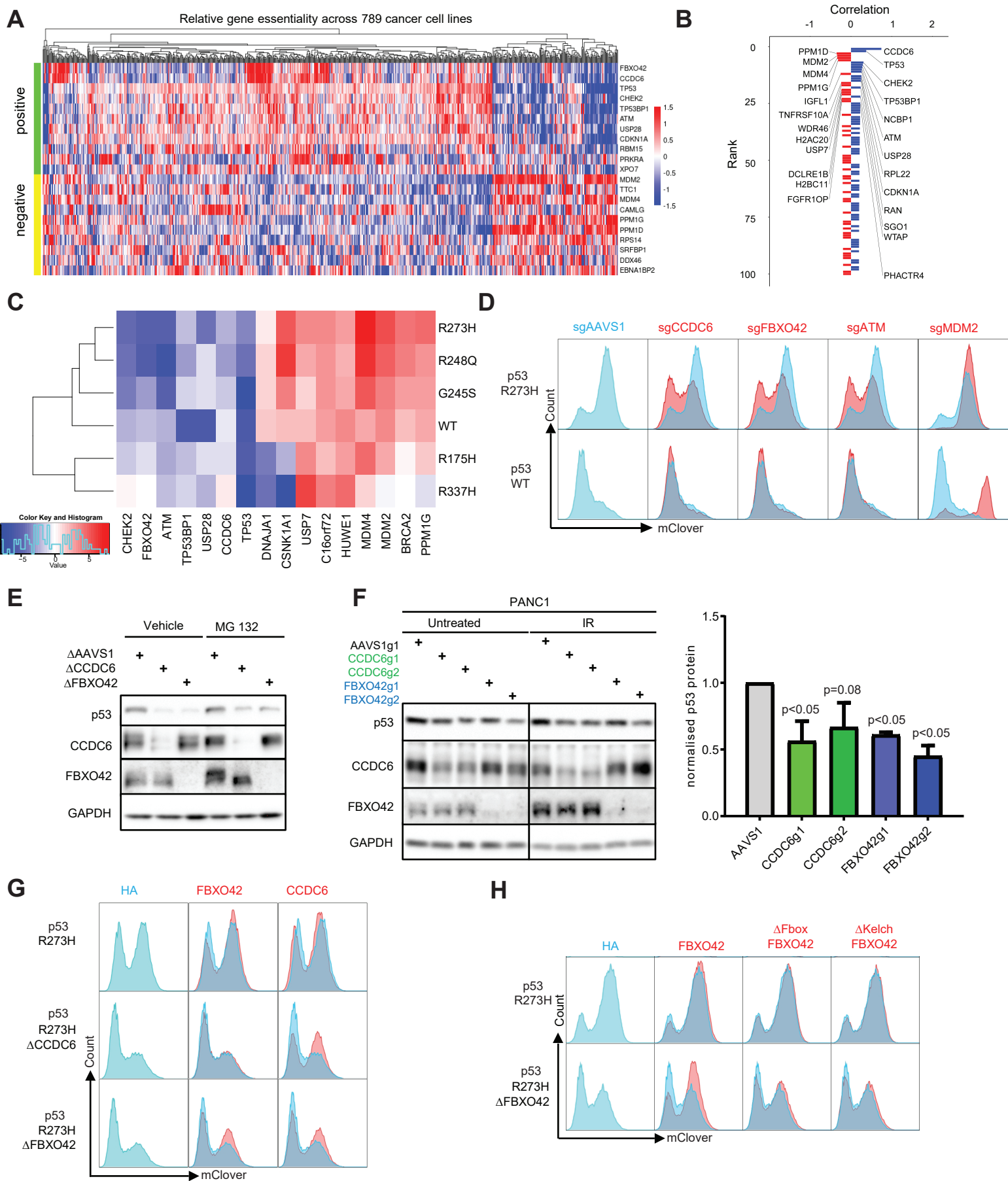


Figure 2. FBXO42-CCDC6 axis regulates mutant p53 protein stability.

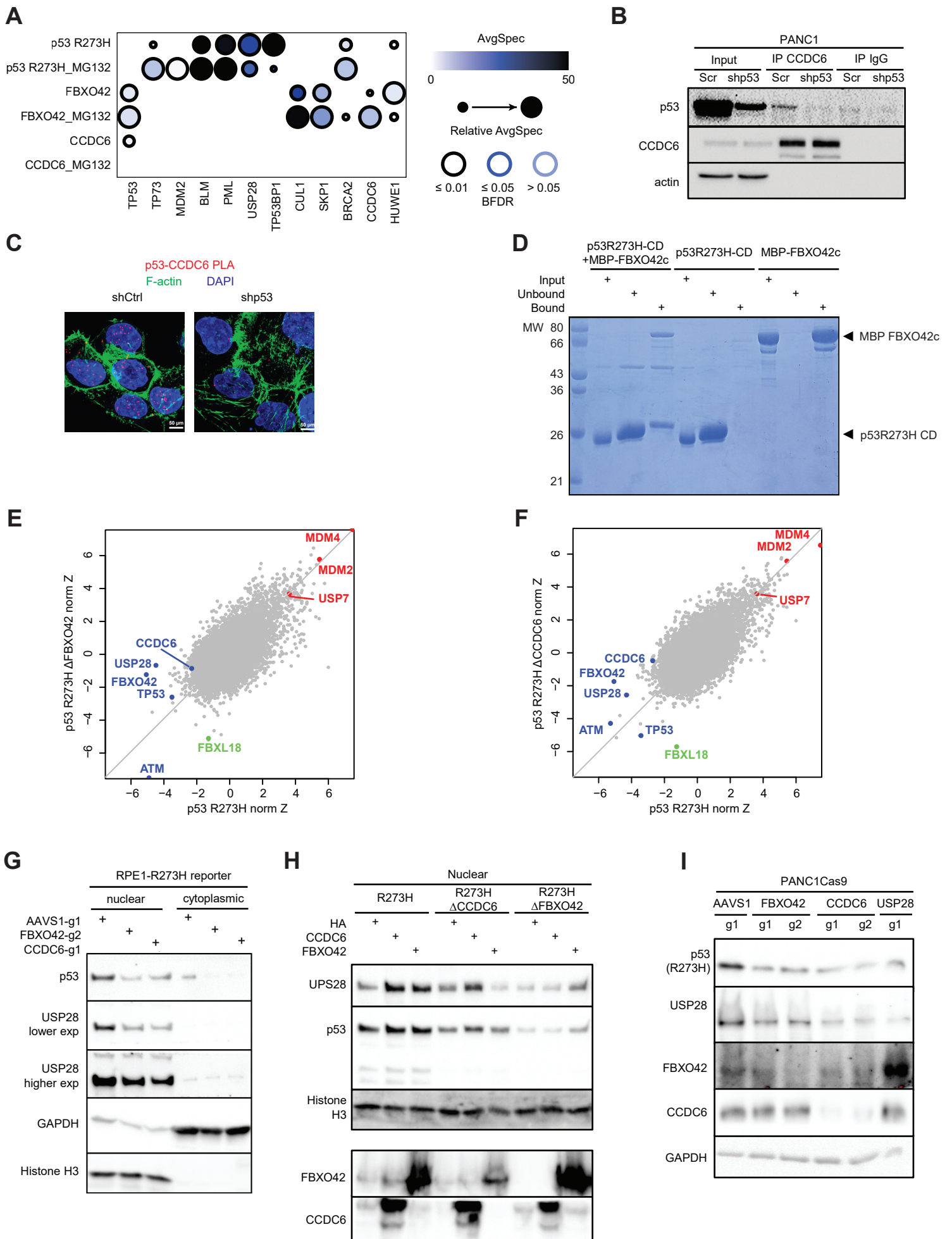


Figure 3. Mapping genetic interactions of FBXO42-CCDC6-R273H

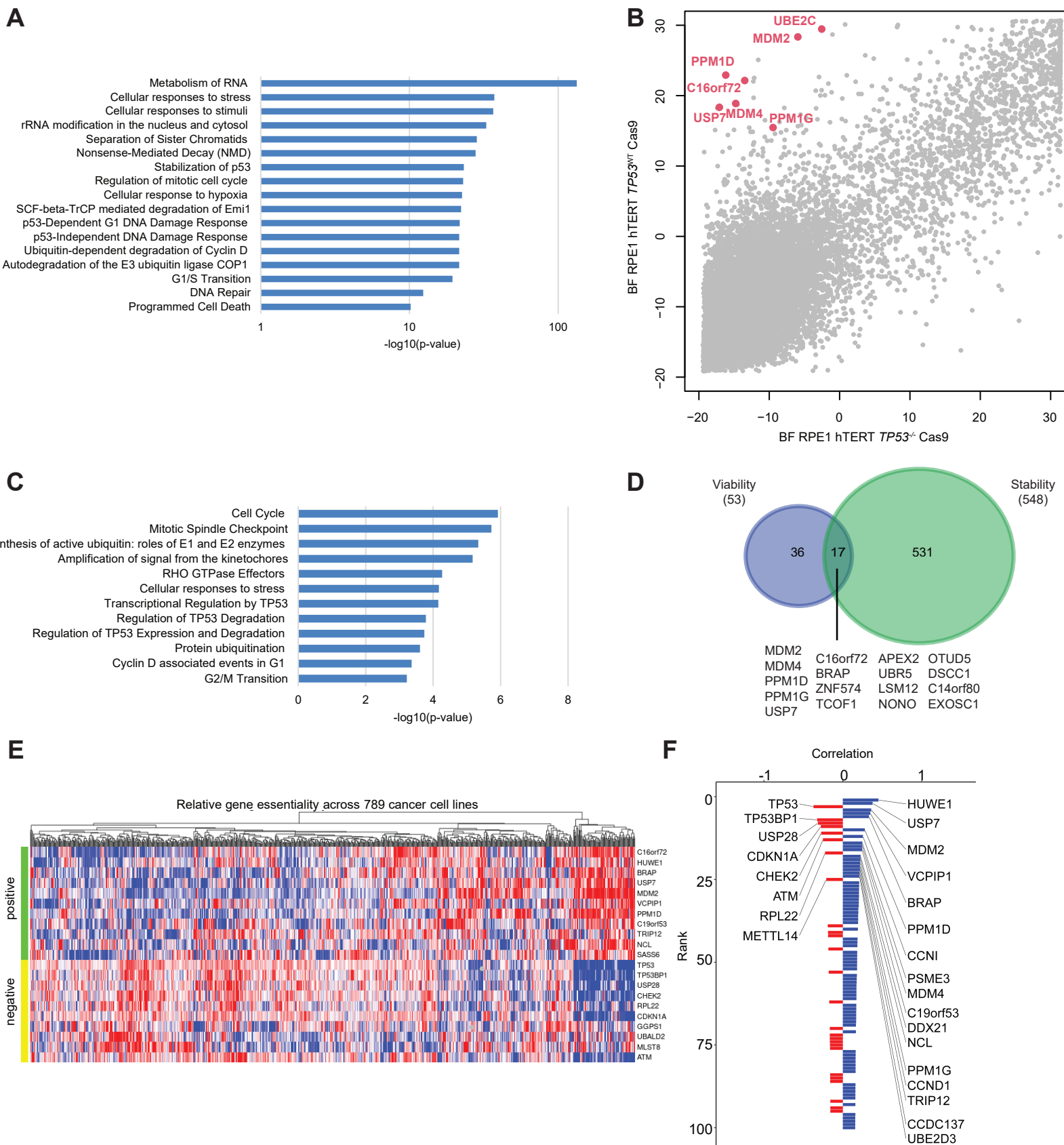


Figure 4. Synthetic viability screen maps regulators of p53.

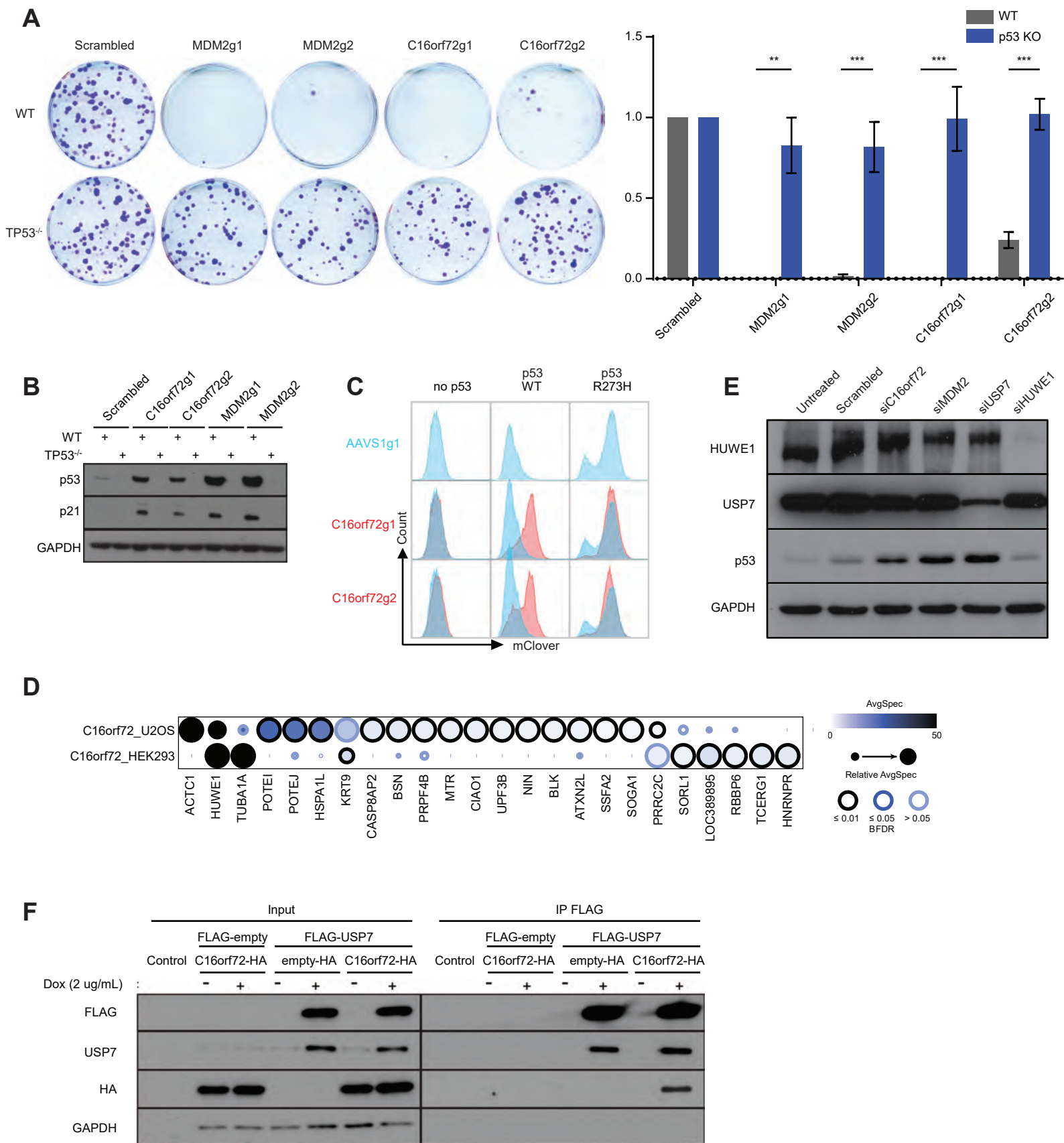


Figure 5. C16orf72 is a regulator of wildtype and mutant p53 stability.

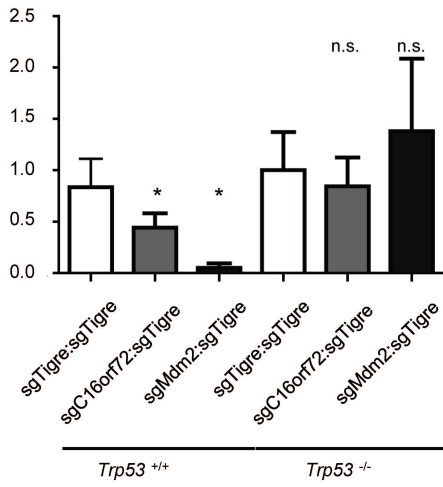
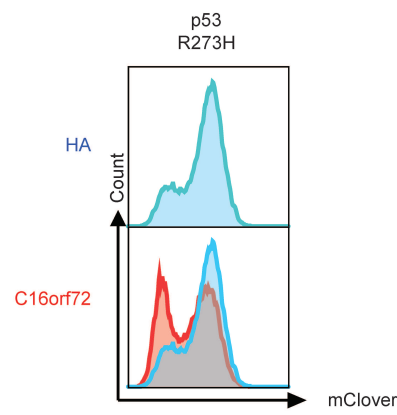
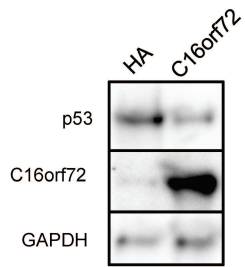
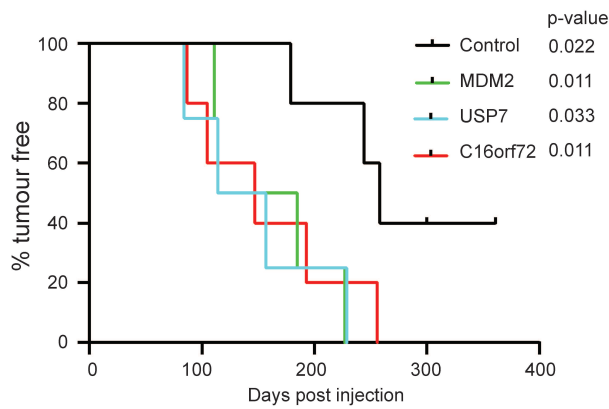
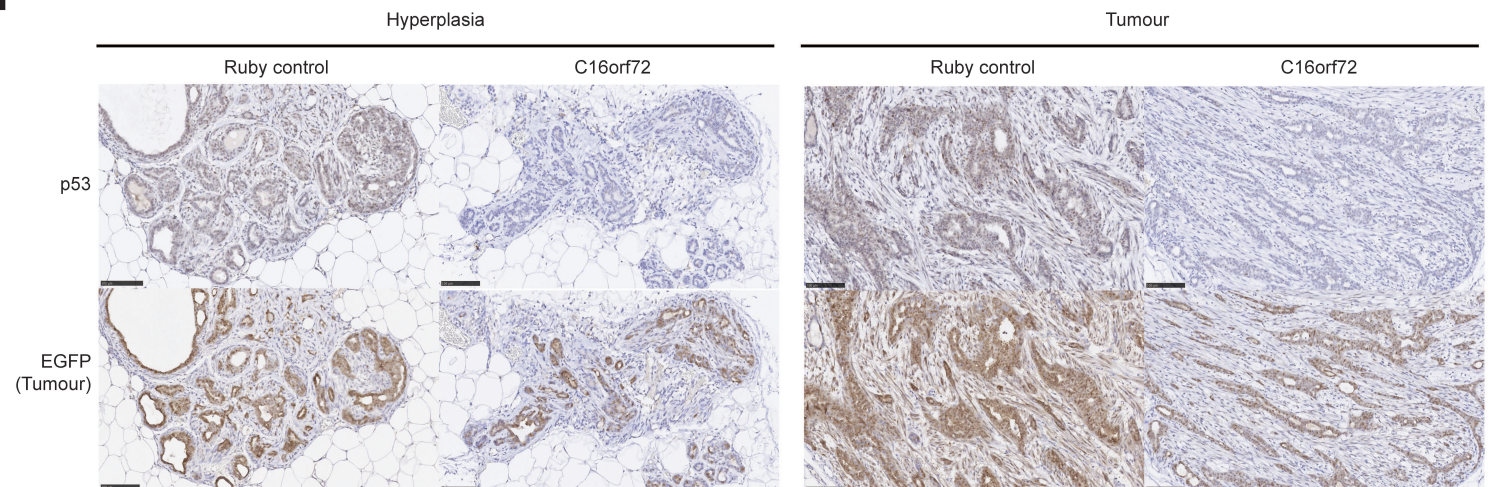
A**B****C****D****E****F**

Figure 6. C16orf72 functions as oncogene and regulates p53 stability in the mammary gland.